POLITECNICO DI MILANO

School of Industrial and Information Engineering

Master of Science
in
Physics Engineering – Nano Optics and Photonics

Design and Optimization of a Compressive Sensing Time Domain Raman Spectrometer (CS-TDRS) for fast probing of thick diffusive media

Supervisor: Prof. Antonio PIFFERI

Assistant Supervisor: Dr. Sanathana KONUGOLU VENKATA SEKAR

Author:

Michele LACERENZA
Nr. 874703

Academic Year 2017 - 2018.

CONTENTS

ABSTRACT

In recent years, Diffuse Raman Spectroscopy (DRS) is emerging as a new tool for studying biological diffuse media with a high degree of innovation. Thanks to its high specificity to chemical and structural properties of the molecules, it became a unique tool in biomedical diagnosis. Compared to Diffuse Optical Spectroscopy (DOS) based on absorption and scattering techniques, in DRS only one excitation wavelength can generate broadband Raman lines, giving the possibility to retrieve molecular information of diffusive media. The limitation of DRS stays in the Raman signal intensity that can be revealed, this is why it has always been very hard to probe deep tissue throughout Raman scattering. Time domain and frequency domain setups have been tested with successful results making it possible to reach deeper layers of the samples. With this project, we are Introducing a new tool for Time Domain deep Raman probing with the innovative implementation of Compressive Sensing. Thanks to the intrinsic features, sparsity, and incoherence, proper of spectral scenes and detecting structure, it is possible to recover spectral images from fewer measures than common monochromator scanning technique. Due to low number Raman photons scattered from the excited sample, highly costly detection systems such as single photon avalanche diodes (SPAD) with high efficiency in the near infrared region are required. This set up usually takes to an off-budget final system. By the design and set up of a compressive sensing (CS) spectrometer, exploiting the features of a Digital light processor (DLP), it is possible to greatly increase fastness in Raman spectral imaging. CS detection will enable to use single-pixel cameras to retrieve full Raman spectra, drastically decreasing costs. It will be possible to implement innovative diffused optics techniques in the time domain, therefore, having chemical specificity and deep probing in tissues within a very short measuring time. In this thesis are shown the design, the construction and the characterization of the Compressive sensing – Time Domain Raman spectrometer and the results of the first measures on thick diffusive multilayer phantoms.

1 CHAPTER 1 – INTRODUCTION

" A small journey through the understanding of matter. "

This is what comes into my mind when I think about my thesis project. I decided to undertake such a journey after many months of thinking and comparisons between other similar projects. I have always been interested in discovering how things work, how they are made, and when I came through optics, I suddenly found a discipline that made me able to "talk" directly with the objects that were under my spotlight. Light waves or photons are like words that make up a full language and enable us to transfer and receive information with the outside world. We can manipulate light and light can be changed in very peculiar ways related to the object on which it is impinging. By understanding how matter changes light it will be possible to interact with it and discover a whole new world. The main issues deriving from the will of talking with mater are two. The first one is being able to detect this changes generated by the interaction of light and mater and the second Is to understand it.

The aim of this project Is related to the first issue. In fact, it will eventually be developed a new homemade device that will help to detect changes in light produced by the light-matter interaction. A particular physical effect will describe the changes in light that will give us chemical and spatial information on the sample under study. It is called by the name of the scientist that discovered it: Sir Chandrasekhara Venkata Raman.

In our case, matter talks to us by absorbing the light beam we use to stimulate it and sanding back a shifted wavelength light. Raman spontaneous scattering is the phenomena that we will take into consideration and it is ruled by probability laws and can be explained in theory by exploiting particular diffusion equations. Thanks to the specificity of the spectra generated by Raman effect, it can be possible to reveal patterns of scattered light at a different wavelength that generates the fingerprint of specific chemical components. Shifted wavelength Raman photons are difficult to reveal because they are the consequence of very less probable collisions with molecules but they can bring a lot of information

on the sample chemical composition. The aim of the device that will be depicted in the following pages is to reveal those photons in a fast and efficient way, eventually retrieving precious information on the sample under study.

The whole project can be divided into 4 main parts: In the first part, the characterization of a pulsed and tunable Ti-Sa Laser is shown, this laser is used as excitation beam to induce Raman effect. The design of the CS-TDRS is described in the second part, followed by the characterization of the completed system, third part. The last step is focused on the application of the device, compressive sensing measures in the time domain of thick multilayer diffusive media.

1.1 RAMAN SPECTROSCOPY

In the following chapter, some insights into the theory and principles of Raman Spectroscopy will be shown, if wanted, the references reported throughout the text can help to deepen the understanding of the phenomena.

1.1.1 Principles of Raman scattering

When photons are scattered from an atom or molecule, most of them undergo elastic scattering. Between many types of elastic scattering, let's focus on Rayleigh scattering. After this process, photons have the same energy, frequency, and wavelength, as they had in the beginning. A small fraction of the scattered photons, approximately 1 in 10 million are scattered inelastically, those photons have frequency and energy different from the incident ones.

A spectral analysis of the scattered light under these circumstances will reveal spectral satellite lines below the Rayleigh scattering peak at the incident frequency. Such lines are called "Stokes lines".

If there is significant excitation of vibrational excited states of the scattering molecules, then it is also possible to observe scattering at frequencies above the incident frequency as the vibrational energy is added to the incident photon energy. These lines, generally weaker, are called anti-Stokes lines. Since at room temperature the population state of a molecule is principally in its ground

vibrational state, the largest of the two processes is the Stokes scattering. Whereby those photons are scattered at lower energy, shifted wavelength towards the red end of the spectrum, those are the photons we will look at. Without altering the effect with other physical phenomena, the spontaneous generation of Stokes and anti-Stokes lines is called spontaneous Raman Scattering.

Vibration lines observable with spontaneous Raman scattering depend upon the geometry (symmetry) of the molecule, only some of the vibration levels will be shown. Sufficient information is usually present to enable a very precise characterization of the molecular structure.

Raman effect is described as an inelastic scattering of a photon off of a molecular bond. From the Jablonski diagram shown in *[Fig. 1]*, It is possible to appreciate an energy sketch of the tree effects explained above. In all three cases, the exiting light brings the molecules to an excited virtual energy state. The way the molecule relaxes to lower energy state defines the type of effect that is generated.

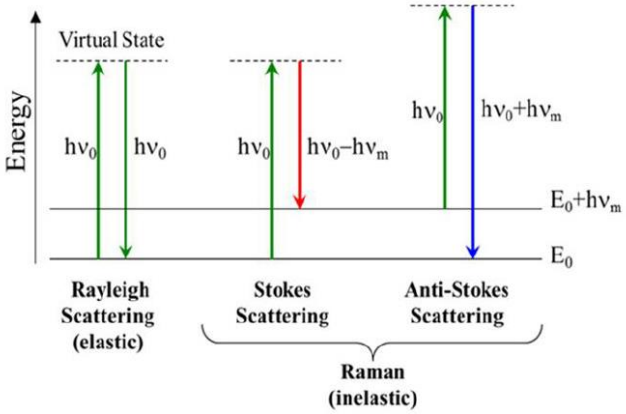

Fig. 1 Jablonski diagram, showing three possibel outcomes atrer the exitation of the molecules to a virtual state. Raylight Elastic Scattering, Stokes Raman Inelastic Scattering and Anti-Stokes Raman inelastic Scattering are presented.

When this occurs, there are three different potential outcomes. First, the molecule can relax back down to the ground state and emit a photon of equal energy to that of the incident photon; this is an elastic process and is again referred to as Rayleigh scattering. Second, the molecule can relax to a real phonon state and emit a photon with less energy than the incident photon; this is called Stokes-shifted Raman scattering. The third potential outcome is that

the molecule is already in an excited phonon state, is excited to a higher virtual state, and then relaxes back down to the ground state emitting a photon with more energy than the incident photon; this is the so-called Anti-Stokes Raman scattering.

1.1.2 Principles of Raman spectroscopies

Raman spectroscopy is a molecular spectroscopy based on inelastically scattered light, it allows for identification of vibrational (phonon) states of molecules. As a result, Raman spectroscopy provides an invaluable analytical tool for molecular fingerprinting as well as monitoring changes in molecular bond structure (e.g. product formation; state changes and stresses & strains; crystalline form and crystallinity).

In comparison to other vibrational spectroscopy methods, Raman has several major advantages. These advantages stem from the fact that the Raman effect manifests itself in the light scattered off of a sample as opposed to the light absorbed by a sample. Raman spectroscopy requires little sample preparation, most of the time sample preparation is even not needed, and it is insensitive to aqueous absorption bands. This property of Raman facilitates the measurement of solids, liquids, and gases not only directly, but also through transparent containers such as glass, quartz, and plastic.

Raman spectroscopy is highly selective, it permits it to identify and differentiate molecules and chemical species that are very similar, and measure small changes in samples. Raman spectra, thanks to anti-Stokes but mainly Stokes lines give us the fingerprint of many kinds of molecules that are different from each other, not only in their composition but also on their geometry. By connecting molecules to their Raman spectra it will eventually be possible to understand the chemical components of a complex sample. In *[Fig. 2]* it is possible to see the fingerprint (Raman Spectra) of a particular material: Cinnabar.

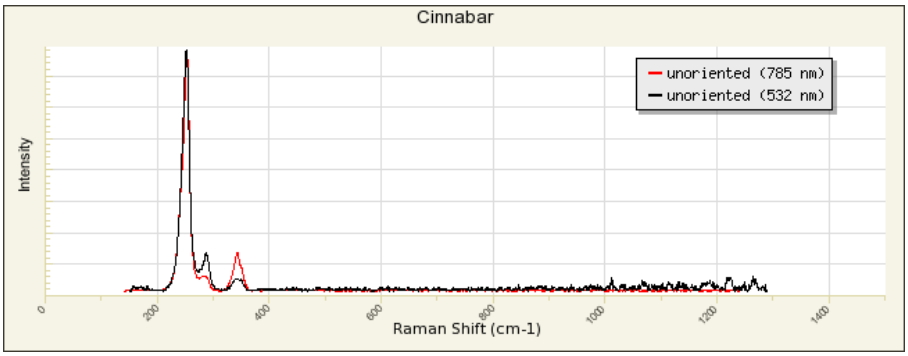

Fig. 2 Cinnabar raman spectra _ http://rruff.info/Cinnabar/R070532

As it can be seen from the picture, Raman spectra are plotted over the wave number, not wavelength. Raman shifts are also in terms of wavenumbers and they are relative to the exiting wavelength. Raman Shifts are set by the molecular feature and are constant related to the excitation wavelength, but the absolute position of the peak in terms of wavelength depends on the excitation frequency. Normally the intensity of the excitation peak is so high that can burry Raman signal, this is why in Raman spectroscopy is absolutely needed to filter out the excitation beam. One other problem of the Raman signal, that mainly occurs when analyzing biological samples is fluorescence. The fluorescence of the sample itself can affect negatively the Raman signal intensity especially when it broadens spectrally. Fluorescence can be subtracted in different ways, either by filtering it, by characterizing it for the specific sample and erasing it from the revealed spectrum or by working in the time domain, because it has very different time behavior compared to Raman signal, they can be therefore temporally divided.

1.2 DIFFUSE OPTICS

In transparent media, light propagates through the material without undergoing scattering with particles or better saying, with a very low number of scattering events. In this case, the intensity of light coming out from the medium will only be affected by absorption and photons will travel in straight lines. Beer-Lambert law [$I = I_0 e^{-\mu_a L}$ Eq. 1] was proposed to explain absorption in such a medium.

$$I_1 = I_0\, e^{-\mu_a L} \qquad \textit{Eq. 1}$$

Where

When the number of scattering centers in a medium increases, the photons encounter more scattering events along with absorption. The medium is said to be diffuse when the number of scattering events of light traveling through the material is relatively higher than the number of absorption events. The scattering centers in diffuse media scramble the photon paths in random directions. At the microscopic level, these scattering centers are particles with a size comparable to the wavelength of light, irregular shapes, different optical properties (absorption, refractive index) compared to its background. This inhomogeneity at the microscopic level in a scale comparable to the wavelength of light gives rise to diffusive spread of light at the macroscopic level. In clear media, the absorption coefficient can be derived from Lambert-Beer law as follows $\mu a = -\frac{ln(I_1/I_0)}{L}$ Eq. 2]:

$$\mu_a = -\frac{ln(I_1/I_0)}{L} \qquad \textit{Eq. 2}$$

Where μ_a is the absorption coefficient, I_1 is the intensity of the beam coming out of the sample, I_0 is the intensity of the beam before entering the sample and L is the total path inside the material. Whereas in diffusive media, dumping of light intensity is due to both scattering and absorption coefficients. In this case, photons undergo complex paths and more sophisticated analysis must be developed A complex light propagation model is needed to characterize the absorption and scattering coefficients of a diffusive medium. "Photon Migration" is a term used by the physicists to refer to the light propagation in diffuse media.

1.2.1 Generalities on Diffuse Optical Spectroscopy

Diffuse Optical Spectroscopy is a technique to extract optical properties (absorption μ_a, reduced scattering μ'_s) of a diffusive media [1]. $(\mu_\sigma)^{-1}$ and $(\mu_s)^{-1}$ are defined as the absorption free mean path and scattering-free mean path respectively. The reduced scattering coefficient is a property incorporating the scattering coefficient μs and the anisotropy g:
μs' = μs(1 - g) [cm-1] . The purpose of μs' is to describe the diffusion of photons in a random walk of step size of 1/μs' [cm] where each step involves isotropic scattering. Such a description is equivalent to the description of photon movement using many small steps 1/μs that each involves only a partial deflection angle θ (g = <cos θ>) if there are many scattering events before an absorption event, i.e., μa << μs'. This situation of scattering-dominated light transport is called the diffusion regime and μs' is useful in the diffusion regime which is commonly encountered when treating how visible and near-infrared light propagates through biological tissues. Most of the in vivo biological tissues are diffusive in nature. Thus, a broadband spectroscopy on in vivo tissue followed by comparison with individual spectra can quantify the key tissue chromophores in the measured location.

1.2.2 CW multi-distance

Continuous waves spectroscopy analysis can be very interesting when it comes to discovering optical properties of an analyzed sample and even diffused optical tomography. In fact from the different absorption properties of materials, various elements can be discerned in a complex sample relates to their position and concentration. If for example a small element with high absorption is ubicated inside a low absorption thin scattering sample it will be possible to recover the position of the inclusion by canning the surface of the sample.

By exploiting variable spatial offset continuous wave techniques it is also possible to scan different depths of a specific sample, due to the diffusion photon path inside of a scattering medium. In fact, photons in a scattering medium injected into a surface point A and collected from a detection point B will follow a path ruled by the probability of absorption and scattering events. The most probable path is the typical banana shape path of the

photons *[Fig. 3],* an accurate analysis of the probability of the different path can be studied for example trough Montecarlo simulations. In this special offset spectroscopy, it has been seen that the more the points A and B are apart from each other, the more probable is for photons to reach deeper layer. Deriving from this assumption it will be possible to scan dip layers with increasing spatial distance.

1.2.3 Time Domain

A system for time-resolved photon migration measurements requires a pulsed light source (typically a Mode-Locked laser) and detection electronics with sub-nanosecond temporal resolution and sensitivity at or near the single-photon level. From single photon counting devices, it is possible to reconstruct curves representing the number of photons impinging on the detector on the time scale of one laser pulse (hundreds of ps). These curves are called photons time of flight curves (TOF). Upon propagation into diffuse media, due to the absorption and scattering, the laser pulse gets broadened. To be more specific, the absorption (μ_a) affects the slope of the pulse tail, whereas the scattering (μ'_s) shifts the peak. Thus, TD naturally decouples the optical properties (μ_a; μ'_s). The retrieval of the mean optical properties of the elements under analysis is also possible exploiting the analytical solution of the radiative transfer equation under the diffusion approximation for different geometry [2]. Fitting the supramental curve and the theoretical behavior is possible to retrieve optical properties. Time-Domain Diffuse Optical Spectroscopy (TD-DOS) has been realized in different configurations. With the advancement of technology in the field of source and detectors, the TD-DOS has been evolved from a laboratory-based system to a hand-held compact device [3].

1.3 DIFFUSE RAMAN

Raman spectroscopy is a consolidated technique widely used in probing nondiffusive media. Only in recent years, RS is emerging as a new tool to study

biological diffuse media with a high degree of innovation [4 5 6]. Thanks to its high specificity to chemical and structural properties of the molecules it became a unique tool in biomedical diagnosis. Compared to diffused optical spectroscopy (DOS), diffused Raman scattering trough only one excitation wavelength can generate broadband Raman lines, making us able to retrieve molecular information of diffusive media. The limitation of Diffused Raman Spectroscopy (DRS) is the Raman signal intensity that can be produced. In fact, the Raman lines have an attenuation of six orders of magnitudes compared to the excitation intensity. Fortunately, the detection system's technology is advancing faster every year and detection efficiency is facing great improvements. Fluorescence of biological tissues is also not negligible in DRS because it can easily cove Raman signal. But, by selecting suitable red shifted Raman exiting wavelength, the fluorescence they overwhelms the Raman signal can be strongly reduced. As in DOS, time domain and frequency domain setups have been tested in Raman with successful results. I will mainly focus on the description of Spatial Offset Raman Spectroscopy technique (SORS) where depth selectivity is achieved by changing source-detector separation and Frequency Offset Raman Spectroscopy technique (FORS), a very new technique where different optical frequencies are used to achieve depth selectivity thanks to the diverse optical property of multilayer samples.

1.3.1 Sors

SORS is the older technique between the two, it was born in 2005 and it has been tested and studied deeply. In this approach, a spatial offset is imposed between the exiting beam and the detector, making the offset variable, it is possible to scan different depth of the material under study. Raman spectra observed on the sample surface will have a different relative contribution from the surface and the sub-surface layer. A larger source-detector separation carries information on the deeper layer of the sample *[Fig. 3]*, this behavior is ruled to the photon path inside the analyzed material. This feature is very powerful when it comes to in vivo tissue spectroscopy. The numbers of detectors coupled to one emitting source can vary and they can be placed in different forms, usually, when many detecting points are exploited, they are located on a circumference of radius r around the source (r will be the spatial offset). The surface fluorescence contribution, that would normally cover the

Raman signal, can now be avoided by increasing the source-detector distance. The technique has been proved to be very powerful even at a commercial level, we can see it in many applications such as clinical diagnostics of breast cancer [7], bone diagnosis [8], pharmaceutical quality control [9], explosive detection in airport [10]. However, SORS suffers from low spatial resolution due to measurements at multiple source-detector separations and low signal to noise (SNR) ratio at large r.

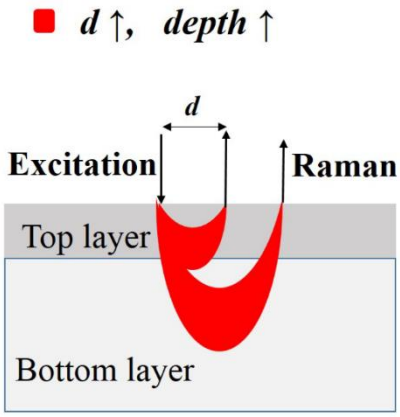

Fig. 3 Most probable path, in scattering media. Increasing the source detector distance, deeper layer can be probed.

1.3.2 Fors

FORS Is a new technique very promising in Raman spectroscopy. The fundamental principle of FORS is based on the dependence of the optical properties of a medium on the exciting wavelength. As optical properties, we take into consideration the absorption and scattering coefficients (μ_a, μ_s). The mean penetration depth of the photons collected at a distance d from the source injection point is a variable of the optical properties (μ_a, μ_s) of the medium. Hence, depth probing can be realized by exploiting the different values of the optical properties of the medium at different excitation frequencies. By acquiring Raman spectra at various excitation frequencies it is possible to selectively probe different depths of the medium. In highly scattering or diffusive media, high absorption impedes photons propagation in the deeper substrates. In fact, if the top layer is characterized by high absorption, it is very hard to probe lower layers but by changing excitation frequency, to a region

where the scattering properties of the material are lower, it will be feasible to make the photons explore deeper layers. This suggests that in a bilayer system, the bottom layer signal can be enhanced by exploring spectral regions where the scattering properties of the medium are weaker. In brief, maximum scattering contrast versus excitation frequency enables maximum contrast of Raman signal between the top and the bottom layer.

1.4 State of the Art of Time-domain diffuse Raman

Spontaneous Raman spectroscopy is rapidly evolving in recent years. In transparent media, RS is already consolidated and many different techniques have been implemented with verified effectiveness. A microscope is often included in the setup in order to increase the collection efficiency of scattered photons. A confocal microscope translated on the z-axis with respect to the sample plane can also be used to achieve depth selectivity in clear media. In diffusive media, however, both the excitation photons and the Raman photons will undergo multiple scattering events in all directions. Focusing on deeper layers and achieving depth resolution is therefore problematic. New solutions have been raised to selectively probe Raman spectra of deeper layers approaching different physical domain to overcome the problem: temporal, spatial and frequency domain.

Studies in the temporal domain raised from the fact that the inelastically scattered component of light (Raman) decays substantially more slowly than its elastically scattered counterpart (laser light). From the knowledge of diffuse optics, it is also known that photons exiting the sample at later times have traveled in deeper sections of the sample, thanks to numerous scattering events. A pulsed exiting source produces Raman pulses coming out of the sample from which photons TOF curves can be retrieved. By gating in time the curves, information on deeper layers can be found in late photons and early photons will show the contribution of superficial layers. Time domain Raman spectroscopy has is also a promising solution to the fluorescence issue. Unfortunately, the measured Raman spectrum is

typically masked by a strong fluorescence background in most potential applications. This is due to the fact that the probability of Raman scattering (cross-section) is much lower than that of fluorescence [11] [12]. By "time-gating" the measurement to the duration of the laser pulse, the total intensity of the fluorescence in the recorded spectrum can be substantially reduced. This results in an improved signal-to-noise ratio and/or shorter measurement time, since the photon noise of the recorded fluorescence emission, which is proportional to the square root of the fluorescence baseline intensity, is now markedly reduced.

Raman spectrometer measurement set-ups that employ the above time-gating principle can be achieved in different ways. Detectors are of main importance in that TD device, some examples of the state of the art of TD system are presented in the following lines.

A high-speed optical shutter based on a Kerr cell is used to realize the time-gate function in [12] and [13], while a photomultiplier and a time gate fulfill the same purpose in [14] the measurement of a time-gated Raman spectrum with a combination of a mode-locked laser, spectrograph and ICCD (intensified CCD) to achieve a 200ps temporal resolution has also been demonstrated [15]. Other more interesting techniques based on measurement of the time position of photons with CMOS SPAD detectors have been used. The time-gating of a CMOS SPAD in Raman measurement was proposed and preliminarily demonstrated in [16], and then also in [17] with a CMOS SPAD 2D array having a minimum time-gate of 700ps. A 2D CMOS SPAD array with even shorter time gate was studied in [18]. Compared with [16] and [17] [18]. Furthermore, have been presented techniques for measuring the complete 2D time interval – wavenumber spectrum of the sample[19].

Although functional in principle and able to demonstrate the potential of the time-gating method, the above systems are either highly sophisticated, physically large and expensive, or capable of measuring only a single wavelength band of the spectrum at a time, so that they require long measurement times and are thus unsuitable for off-laboratory applications. A dramatic reduction in complexity of TD-DRS is expected in the future by the effective use of novel photonics devices like Silicon Photomultiplier (SIPMs) [20]. The impact of TR systems could definitively improve because of the great features offered by these novel devices to obtain depth information [21] [20]. There are few time-domain Raman systems in literature, fast gated cameras [22], ultrafast Kerr

gating [23] time-correlated single photon counting [24] are few examples. Other solutions can be given by a combined usage of multiple detectors, generating for example arrays of SPADs.

In the space domain, we also find the implementation of diffuse optics techniques into Raman spectroscopy, giving rise to SORS *[1.3.1]* spatial offset techniques. In this case, CW lasers are used and depth selectivity is given by variable source-detector distance. Time domain and space domain techniques have also been brought together in some interesting work where the objective was to use of time-resolved (TR) Raman spectroscopy and spatially offset Raman spectroscopy (SORS) to obtain high-quality Raman spectra from materials hidden underneath an opaque. Time-resolved mode was achieved using an intensified CCD camera with a 250 ps gate [25]. By using SORS technique to probe deep layer, we are forced to change the source-detector distance, therefore, loosing spatial (on plane) resolution (it does not happen with TD techniques where the inter-fiber distance can stay constant, zero inter-fiber distance will give maximum spatial (on plane) resolution)

The frequency domain approach is the most novel technique where depth selectivity is achieved thanks to different optical properties of the material. Different excitation frequencies are used to probe different depths. Frequencies that are less scattered and less absorbed by the upper layer will be used to probe deeper substrate of the sample. The approach has already been demonstrated experimentally [5] on a two-layer tissue phantom and compared with the already consolidated spatially offset Raman spectroscopy (SORS) technique. In one other very recent work time domain techniques have also been implemented in FORS setups [26] reaching very good results.

1.4.1 Insights on Time domain Raman diffusion theory

In the following paragraph, only some insights are presented on Raman diffusion theory, in order to give a general introduction to the issue. The interested reader is invited to focus on references for deeper and more accurate information.

It is fundamental to the development of rigorous mathematical models for the Time-domain systems. Simulations based on theoretical models can serve as a support in the development of novel measurement methods or in the understanding of the physics of Raman photon migration and propagation in diffusive media. In literature, it is possible to find works where rigorous modeling of Raman photon migration in Diffusive media based on the diffusion approximation (DA) to the Radiative Transfer Equation (RTE) have been recently developed [27].

Origin of Raman scattering is different from that from Rayleigh scattering. In Raman case, the effect is generated from inelastic intrinsic nature of the molecules, whereas the latter depends on the microscopic structure if medium and the interaction is elastic in nature. Hence Raman scattering involves the change in photon direction and also the wavelength, we need a couple of RTEs to deal with two different wavelengths. Light propagation in biological tissues and other highly scattering media can be modeled with the time-dependent diffusion equation [2] due to the diffusive regime of photon migration that is often utilized in these media. Therefore, the Raman phenomenon can be modeled by two coupled diffusion equations for the time-dependent photon fluence rate. A heuristic model that simplifies the TR-DRS model to TD-DOS model under special conditions has been developed [28].

1.5 Applications of diffuse Raman

Numerous applications of Raman spectroscopy have been discovered during the last decade. From food to airport security and medical diagnosis RS has got a very high potential and can be exploited for materials characterization and analysis with extremely high selectivity.

1.5.1 Pharmaceutics Field

Vibrational spectroscopy is an excellent method for identifying substances because it provides fingerprint spectra that are unique to each specific compound. Semple preparation in Raman spectroscopy is nearly inexistent, this makes it ideal for the analysis of tablets, powders, and liquids, thus avoiding mechanical changes during sample preparation, which could alter the physicochemical properties of the formulation. However, although Raman spectroscopy shows trends in analytical chemistry and advantages over the more traditional IR spectroscopic techniques, it should not be considered as ''the'' analytical technique to solve most problems, but as one more powerful technique that is part of a multidisciplinary approach to analysis. As Raman spectroscopy enables rapid, non-destructive measurements, the technique appears a most promising tool for on-line process monitoring and analysis in the pharmaceutical industry [21] [29] [30].

The pharmaceutical analysis may benefit from the advantages offered by Raman spectroscopy in various ways:

1. Identification of raw materials (building up an extensive library of Raman spectra)
2. Quantitative determination of active substances in different formulations;
3. Supporting polymorphic screenings (polymorphs have different solubility rates, thereby impacting the effective dosing)
4. Supporting chemical development process scale-up (as process steps are modified and refined to ascertain whether the same form of the same chemical is being produced or not).

1.5.2 Airport Security

The rapid detection, in situ, of illicit drugs is a key issue in the forensic and security arena. Most street samples that are routinely analyzed are often impure and contaminated with a range of cutting agents. Their identification requires time-consuming chemical extraction and subsequent laboratory analysis.

Raman spectroscopic analysis of illegal drugs has until recently been confined to the laboratory, however, technological advances have afforded the ability to miniaturize many of the components found in dispersive instruments; near-infrared (NIR) diode lasers, charge coupled detectors (CCD) and fiber-optics. These developments in addition to spectral identification software have facilitated the commercial availability of portable Raman spectrometers for in-field applications. In many airports now Raman chemical recognition is applied to the detection of illicit contraband in the form of drugs-of-abuse [30] [31].

1.5.3 Food

Rama spectroscopy has now been widely studied also in molecular recognition of food, in order to detect chemical features related to the quality assessments of food [32]. Not only traditional Raman food-applications have been studied, but also implementing phenomena on the nanoscale, such as surface-enhanced Raman scattering [33]. Quality control in industrial food processing and food safety in agricultural plant production are just some of the possible applications of Raman effect in the word of food.

1.5.4 Cultural Heritage

Also in cultural heritage, Raman spectroscopy has found its application. Studies have been carried out with many Raman spectroscopy technique as for example SORS [34] and FORS [35]. In this field, Raman spectroscopy is used as a fast and extremely exact way to make a chemical analysis of paintings or sculptures. Being Raman spectroscopy noninvasive and with no need of sample preparation, it is a perfect solution in the field of Arts and cultural heritage [36]. By discovering the composition of the paints used in a painting [37] or manuscripts [38], even at different depth, it can be possible either to date it in time or to discover previous versions underneath the superficial paint and even analyze chemical components that have been used in constructions.

1.5.5 Clinical

The key hypothesis underpinning this field is that molecular changes in cells, tissues or biofluids, that is either the cause or the effect of diseases, can be detected and quantified by Raman spectroscopy. Furthermore, multivariate calibration and classification models based on Raman spectra can be developed on large "training" datasets and used subsequently on samples from new patients to obtain a quantitative and objective diagnosis. Historically, spontaneous Raman spectroscopy has been known as a low signal technique requiring relatively long acquisition times. Applications are present in different fields of medicine, many studies have been done for the studying of cancer fingerprint especially on brain, breast, lung, skin, and prostate. For example, the potential of using a fiber-optic Raman probe for in-vivo diagnosis of brain tumors was investigated in this work [39]. Raman spectral maps over areas 3.6 × 3.2 mm^2 allowed label-free diagnosis of induced metastatic brain tumors in mice with an accuracy of approximately 250 µm. Krafft et al. used Raman spectroscopy in the fingerprint region (600–1800 cm−1) to investigate primary brain cell density [40]. For high-grade gliomas, the Raman spectra had a higher contribution from nuclei acid compared to normal tissue. The authors also demonstrated the ability to create Raman spectral images by raster-scanning.

Studies have been led towards the diagnosis of different bone disease as well. Many bone diseases arise because of subtle changes in the bone protein chemistry but these are invisible to conventional techniques like X-rays. Raman spectroscopy is potentially able to detect these subtle molecular changes and its potential to enhance the diagnosis of osteoarthritis, brittle bone disease, and fragility fractures have been investigated. Frequency shifts serve as an important source of contrast in assessing tissue components such as carbonate substitutions for phosphate positions in bone. The extracellular matrix also provides another source of contrast to bone tissue composition. The extracellular matrix contains many protein-rich vibrational modes, corresponding predominantly to collagen features such as amide backbone, protein secondary structure, and side

chain composition. Early studies compared the Raman spectral features of bone with those of their major components, such as hydroxy and carbonated petite [41]. Raman spectroscopy has been used to evaluate alterations to bone composition associated with aging, disease, or injury to aid in the diagnosis and prediction of fragility fractures [42]. Osteoarthritis is a common debilitating disease that results in degeneration of cartilage and bone in the synovial joints. Raman spectroscopy has shown that subtle changes in the molecular structure of the subchondral bone matrix, or inherent differences, exist in both the medial and lateral (beneath intact cartilage) compartments of osteoarthritis knees [43].

1.6 Introduction on Compressive Sensing

Compressive sensing is widely used in image processing and acquisition [44], it makes possible to lower the amount of data required to have the full information to reproduce an acquired image or signal. This is possible thanks to the possibility to select important information that is essential and sufficient to recover the full signal. Imaging spectroscopy involves the sensing of a large amount of spatial information related to many different wavelengths. In Raman spectroscopy, in particular, due to a low number of Raman photons, the time needed to acquire a sufficient amount of light is orders of magnitude higher than in normal spectroscopy. By using Compressive Sensing it could be possible to recover spectral images from far fewer measurement than the ones required by conventional linear scanning spectral sensors (thus lowering measure time). This can be done thanks to the intrinsic feature, proper of spectral scenes: sparsity and incoherence, proper of the detecting structure. Sparsity makes us able to summarize spectral images in some basis W with just a small number of coefficients. In fact, in spectral images, it is possible to find a correlation among confining pixels and also across spectral bands. Incoherence refers to the structure of the sampling waveforms used in compressive sensing that, unlike the signals of interest, have a dense representation in the basis W [45]. In such a way, by mathematically transforming the sensed spectral image, it is possible to retrieve which one are the critical information and lower the total information needed. This transformation can be optically applied to the signal. By spatially

filtering the spectral image, with preselected patterns, it is possible to reconstruct the full spectrum just by a small number of integrated measures rather than a sequential scanning of all filtered wavelength.

Many patterns can be created and tested for the compressive detection, in literature Hadamard patterns have been widely used and proved to be efficient to compress Raman spectra information [46] [44]. Hadamard patterns have got the interesting feature of being made up of logical (0,1) components, it makes them easy to generate and to use. To retrieve formations from the filtering of Hadamard patterns, the Hadamard transform function is used, it is an example of a generalized class of Fourier transforms, and performs as an orthogonal, symmetric, linear operation on 2m real numbers. To be able to reconstruct the signal in a fast way, the fast Walsh–Hadamard transform is an efficient algorithm to compute the Hadamard transform. The computational process is widely used in many compressive sensing systems for image acquisitions as we can see in references [47] [45].

1.7 ORIGINALITIES OF THE THESIS

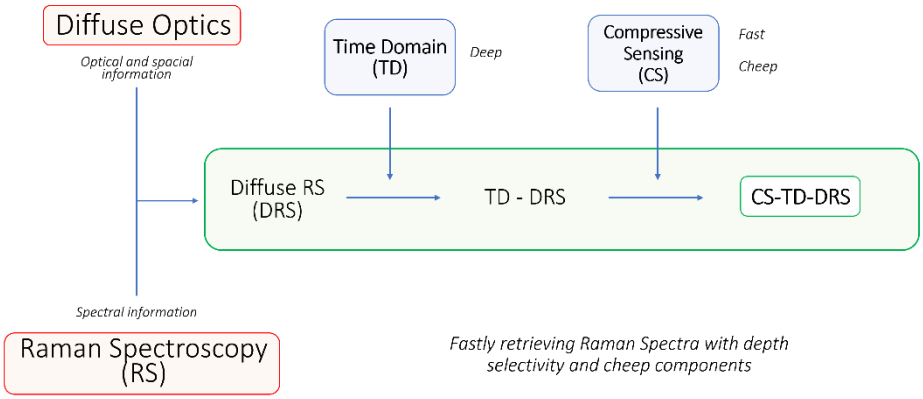

Fig. 4 Sketch showing the different topics contributing to the originality of the project.

Time Domain Raman spectroscopy, has been around for over 20 years but it has never reached high interest due to poor efficiency of the time gating techniques and very costly time domain detectors. Only in recent years, TD measures are becoming of great interest mainly in the Diffuse Optics field. At Politecnico di Milano I have the opportunity to be in close contact with the Diffuse Optic

department where time domain measures in diffusive media are well known and related techniques are widely used mainly focused on Near Infrared Spectroscopy. Acquiring knowledge of TD measures, TD detection system and data analysis will be of great help in the implementation of TD in Raman Spectroscopy.

On the other hand, Compressive sensing implemented in Time Domain Diffuse Raman spectroscopy system is a revolutionary approach that so far it has never been tackled. Due to the low number of Raman photons coming out from an exited sample, some highly costly detection systems such as single photon avalanche diodes (SPAD) with high efficiency in the near infrared region are required. To be able to make images of Raman spectra, matrixes of this costly detectors are needed, usually bringing to an off-budget final system. By using only one single SPAD, the common way of retrieving the full Raman spectra is by scanning all the wavelength with a filtering slit (monochromator scanning) and integrate the outcoming signal each time. Considering that the Raman photons are very few, by filtering the signal on only one narrow band, the intensity is drastically decreased (in our set up, will be 3% of the total light intensity), and the integration time needed to have significant photon counts is increased. It leads to very long acquisition times. By applying compressive sensing to the Raman signal, this problem can be overcome. If particular spatial filters, organized in pattern filtering out just fifty percent of the signal each time, are applied to the spectral image of the Raman signal before the detector, the detected Raman intensity can be increased significantly. By exploiting this method spatial patterns that integrate into time different wavelength will be retrieved. By using Hadamard matrixes as spatial filters, the amount of light impinging on the detector for a given pattern is 50% (for each pattern) of the total light coming into the spectroscope. Thanks to the higher light intensity, for each pattern the integration time can be significantly lowered, compared to the monochromator mode. It will be possible to retrieve the full spectral information with a significantly shorter time of measure (significantly smaller than in the monochromator setup). It will eventually lead to faster acquisitions and cheaper final devices.

The first step of the project will then be the design and the construction of the Compressive sensing Raman spectrometer, working in monochromator mode exploiting spatial light modulator devices, in particular, Digital micromirror devices. Similar setups have already been designed only for CW Raman

spectroscopy as it depicted in ref [44]. The second part of the project will be dedicated to the characterization of the device and finally, the third step will include the application of the CS Raman spectrometer. Firstly it will be used to read the spectrum coming out of high Raman cross-section materials through a microprobe used to collect signal. Secondly, the challenge will be to retrieve Raman spectra from diffusion into the sample that will be eventually double layered samples. In this last case, the aim will be to be able to retrieve Raman spectra of both the materials, the one on the surface and the one underneath.

2 CHAPTER 2 - TI-SAPPHIRE LASER

For the whole project, a tunable laser in the visible and near-infrared region laser was required to facilitate the characterization of the spectrometer and to supply Raman excitation. It has been used a Ti:Sapphire (Ti:Sa) laser modified to accomplish active mode-locking so to combine tunability with fairly narrowband and pulsed operation.

In the following chapter, an analysis in terms of main components and characterization of the laser will be made. In the first part, the solid-state vibrionic laser will be described together with its operating modes. In the second part, an accurate characterization of laser output power properties will be presented.

The Ti-Sa laser is a homemade device, developed at Politecnico di Milano, in our lab. It has been customized as a tunable mode-locked narrowband source tailored for time-resolved Raman signal acquisitions.

The understanding of the laser behavior is critical in order to be able to exploit time-resolved Raman acquisition. The device has got many degrees of freedom for the aligning procedures and it is very sensitive to thermal oscillations, the mode-locked mode is not easy to achieve.

2.1 LASER CAVITY

The laser used is a Ti:Al_2O_3 solid-state resonator working with optical pumping. The pump used is an Nd:YAG laser (Spectra Physics – Millenia_eV) with emission in the green region and variable output power from 0.22 W to 5.00 W (0.2 power accuracy). It is a four-level system, and its inversion population process is shown in *[Fig. 5].*

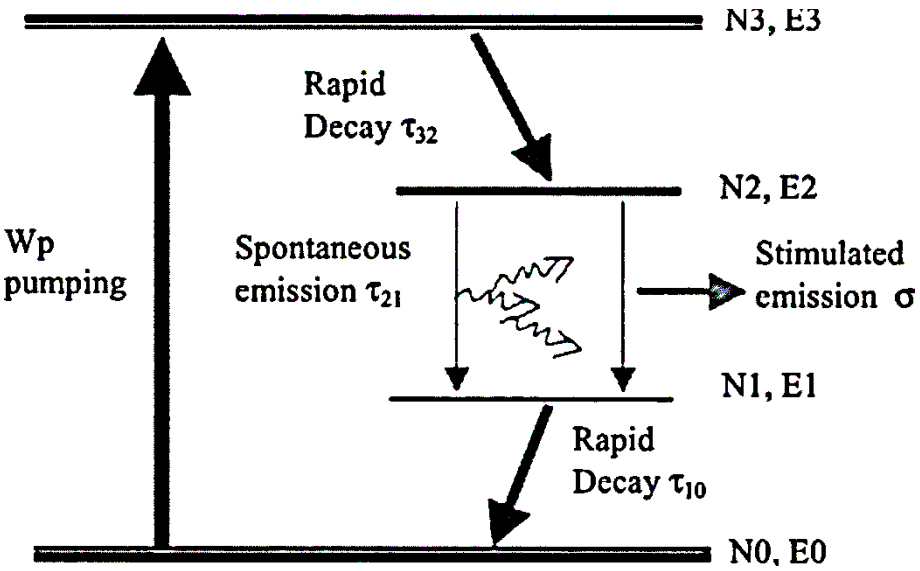

Fig. 5 Sketch of the process of population inversion and Stimulated emission of a 4 level laser system https://www.osapublishing.org/viewmedia.cfm?r=1&rwjcode=josab&uri=josab-21-8-1479&html=true

There are four energy levels: E0, E1, E2, E3, and populations N0, N1, N2, N3, respectively. The energies of each level are such that E0 < E1 < E2 < E3. In this system, the pumping transition P excites the atoms from the ground state (E0) into the pump band (E3). From level three, the atoms again decay by a fast, non-radiative transition into level two. Since the lifetime of the laser transition, 2-1 is long compared to that of 3-2 ($\tau 21 \gg \tau 32$), many atoms accumulate in level 2 (the upper laser level, high-density population), which may relax by spontaneous or stimulated emission into the lower laser level E1, generating population inversion phenomena. This level likewise has a fast, non-radiative decay into the ground state 1-0. As before, the presence of a fast, radiation-less decay transition results in the population of the pump band being quickly depleted ($N3 \approx 0$). In a four-level system, any atom in the lower laser level E1 is also quickly de-excited, leading to a negligible population in that state ($N1 \approx 0$). This is important, since any appreciable

population accumulating in level 2, the upper laser level, will form a population inversion with respect to level 1. That is, as long as N2 > 0, then N2 > N1, and a population inversion is achieved. Thus optical amplification and laser operation can take place at a frequency of v21 (E2-E1 = hv21). Since only a few atoms must be excited into the upper laser level to form a population inversion, a four-level laser is much more efficient than a three-level one where the lower level must be depleted faster to have favorable population ratio (in three-level laser, the laser levels are the ground state and the level one, the level two is the one reached by pump excitation). In reality, many more than four energy levels may be involved in the laser process, with complex excitation and relaxation processes involved between these levels. In particular, the pump band may consist of several distinct energy levels, or a continuum of levels, which allow optical pumping of the medium over a wide range of wavelengths.

The wavelength tunability of the laser is given by a spectral selection system inserted in the optical feedback loop generated by the resonator. This allows the stimulated emission of photons with energy equal to the selected wavelength. In practice, a Lyot filter, inside the cavity length, it is possible to select the emission wavelength. By changing mirrors specifications it is possible to span a broad range of emission wavelengths from 700 nm to 1 µm. During the time period of this research project, the cavity was optimized to have a wavelength range going from 700 nm to 860 nm that is the most interesting range to stimulate Raman emission.

In *[Fig. 6]* it is possible to see the optical configuration of the entire laser system. Only some peculiar elements of the system will be analyzed, to appreciate deeper details see *[ref*[48]*– cap3]*. The plane mirrors

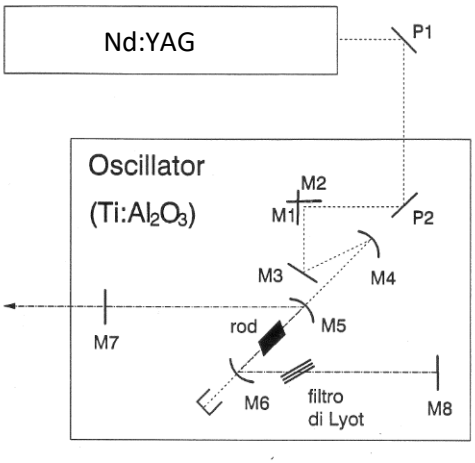

Fig. 6 Ti-Sa Laser [13] Sketch of the optical layout of the cavity and of the laser plus pumping system

P1, P2, M1, M2, M3 are used to bring the pump light inside the resonator with the appropriate polarization. The polarization is rotated at 180° from mirrors M1, M2. The spherical mirror M4 is a crucial component. It is needed to focus the beam on the active material. Its position is variable to optimize the focus on the crystal. Components M4, M5, M, M7 are mirrors core of the resonator. The position of the rod is peculiar, the angle of incidence of the beam is set in order to make the laser beam and the pump beam as much colinear as possible to optimize the inversion process.

2.2 EFFICIENCY VS WAVELENGTH

The Ti-Sapphire Laser has been characterized on its output power versus wavelength. The diode pump has been set to 4W and 3W power in CW and the wavelength has been modified with a wavelength modulator (the Lyot filter) from 700nm to 860nm. The wavelength limits have been set by the features of the resonant cavity hosting the Ti-Sa crystal. The output laser wavelength can be pushed to 690nm but the output power results very low, insignificant. On the other hand, when the wavelength is brought further then 860nm, the laser becomes unstable. Trying to push the laser outside

the stability window, the output wavelength value jumps back and forward of several decades.

The power vs wavelength graphs shows that the laser, facing a constant pump power, provides more output intensity in the range of 780-820nm. It suggests a better laser efficiency in that range. The output power presents a nearly linear increasing behavior from 710nm to 820nm and it decreases from 810nm to 860nm. In case of a lower pump power (3W) the increasing and decreasing behaviors look more gentle, providing a more stable response. It is important to notice that these behaviors are strongly dependent on the mirror set used. Depending on the working wavelength of interest (with relative mirror set) the power vs wavelength behavior can change significantly. The outcomes of the measure are plotted in *[Fig. 7]* where the efficiency has been characterized for two different pump powers 4W and 3W. From now on the standard power used for the pump will always be 4W.

From the graph, it is noticeable that the maximum output power in CW mode is at around 550mW at 850 nm. It has been seen that the maximum output power also depend strongly on crystal temperature and obviously, cavity alignment.

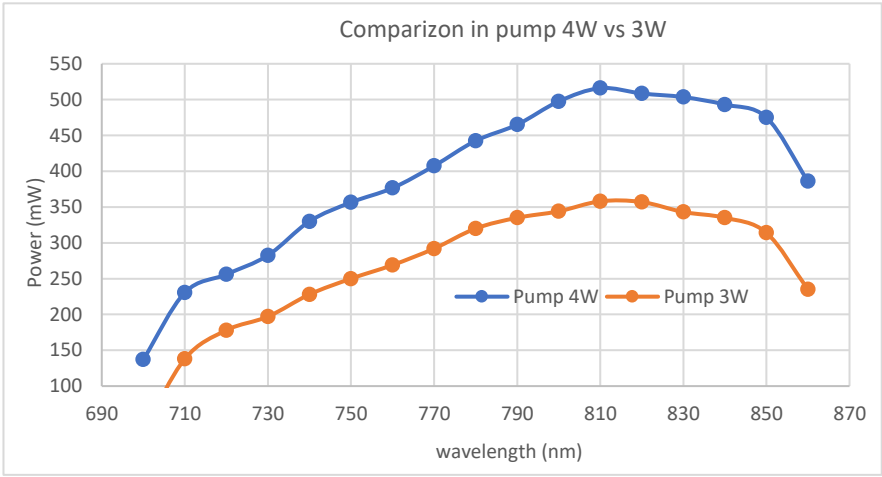

Fig. 7 Power efficiency characterization vs wavelength at two different pump power.

2.3 MODE LOCKING

Mode Locking mode is a particular working regime of lasers where a peculiar condition of interference between modes of the stimulated emission is created. It allows obtaining a train of pulses divided by regular time delays. The condition of interference is set between longitudinal modes of the laser that oscillates in the same region of space. The spectral and temporal behaviors of the pulses are described by Gaussian curves reciprocally related by a Fourier transform. The modes are locked by an Active Mode locking technique that exploits acousto-optic modulation (AOM) of losses when the beam passes through a resonating quartz crystal. The quartz crystal is ubicated in the cavity branch with the incident beam at the Brewster angle and its refractive index is modulated by the acoustic signal coming from a frequency generator at a 100MHz. The modified optical configuration can be seen in *[Fig. 8]*.

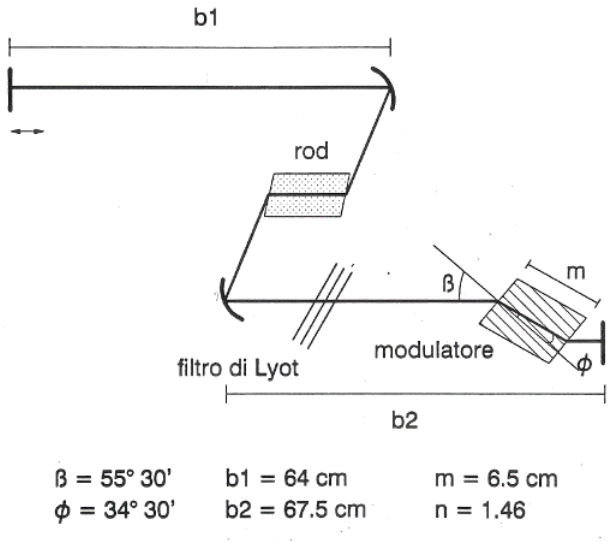

Fig. 8 Modified cavity to achive Mode Locking conditions [13]

The intensity modulation and the frequency modulation are crucial parameters when it comes to pulse intensity and pulse time Full Width at Half Maximum (FWHM).

Going deeper into the mode-locking phenomena, let's consider N longitudinal modes oscillating in the laser cavity, with the same amplitude

E_0. Consider then t=0 s as initial time where all the modes are on phase with each other. Considering, an odd total number of modes N, angular frequency ω_0 of the central mode, and index i running over each mode, it is possible to describe the field generated by each mode with the following equation:

$$E_i(t) = E_0 e^{j(\omega_0 + \Delta\omega_{ax})t} \qquad \textit{Eq. 3}$$

$$\Delta\omega_{ax} = 2\pi \frac{c}{2p} \qquad \textit{Eq. 4}$$

Where $\Delta\omega_{ax}$ is the angular frequency difference between two adjacent modes, c is the speed of light and p is the cavity length.

The interference between all the longitudinal modes generate a total field

$$E(t) = \sum_{i=-\left(N-\frac{1}{2}\right)}^{+\left(N-\frac{1}{2}\right)} E_0 e^{j(\omega_0 + i\Delta\omega_{ax})t} = E_0 \frac{sin(\frac{N\Delta\omega_{ax}t}{2})}{sin(\frac{\Delta\omega_{ax}t}{2})} \qquad \textit{Eq. 5}$$

With relative intensity

$$I(t) = |E(t)|^2 = {E_0}^2 \frac{sin^2(\frac{N\Delta\omega_{ax}t}{2})}{sin^2(\frac{\Delta\omega_{ax}t}{2})} \qquad \textit{Eq. 6}$$

The interference between the phase locked modes will generate a train of pulses. In *[Fig. 9]* the graphic representation of Eq.6 is sown. The time width of each pulse, as the time interval between the maxima of the function and its first zero is given by:

$$\tau_p \approx \frac{2\pi}{N\Delta\omega_{ax}} = \frac{1}{\Delta f_{osc}} \qquad \textit{Eq. 7}$$

Where Δf_{osc} is the bandwidth of laser oscillation. The higher the number of locked modes, the shorter the pulse, in time. The maximum intensity that can be reached for each pulse is given by

$$I_{max} = N^2 {E_0}^2 \qquad \textit{Eq. 8}$$

It is proportional to the square of the number of locked modes.

The interval between two consecutive pulses is given by :

$$\Delta t = \frac{2\pi}{\Delta\omega_{ax}} = \frac{2p}{c} \qquad \textit{Eq. 9}$$

That is the time needed for a complete roundtrip in the cavity.

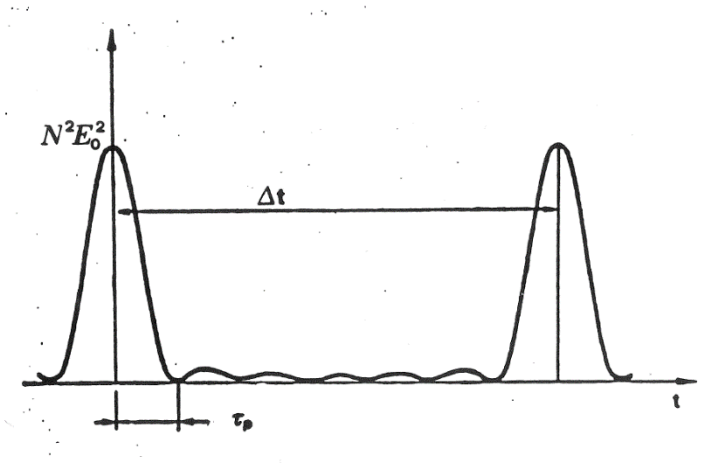

F
i

Same results can be reached with the phasor representation in the complex plane of the electric fields of the modes. In this representation, the superposition of the modes for the generation of the pulse can be visually understood *[Fig. 10]*. Considering the central mode phasor as the reference system, at time t=0, all the modes are superposed, giving a total field $E=NE_0$. With the increase of the time t, phasors move, clockwise or anticlockwise,

with respective angular velocity (multiples of $\Delta\omega_{ax}$). After the time $\tau_p = 2\pi/N\Delta\omega_{ax}$ the phasor have a symmetric disposition on the plane giving a null resultant field. A new maximum is given after $\Delta t = 2\pi/N\Delta\omega_{ax}$ when the phasors are again all superposed.

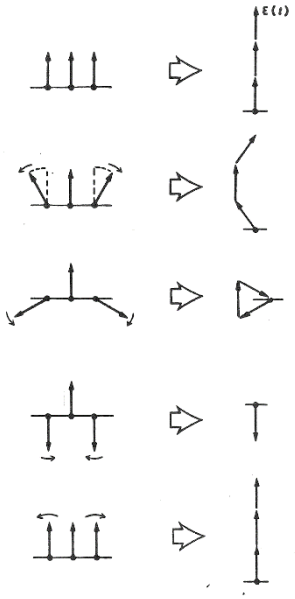

Fig. 10 Vectorial representation of modelocking

To accomplish mode-locking the longitudinal modes are locked by an Active Mode locking technique that exploits acousto-optic modulation (AOM) of losses in amplitude when the beam passes through a resonating quartz crystal. The amplitude modulation is based on the variation of the refractive index of the crystal when crossed by an acoustic modulating frequency f_m. The refractive index depends on the stress state of the crystal. By sending an acoustic wave to the crystal with a particular frequency fm resonant with the material, it is possible to reach a stationary configuration of the stress state (direct and reflected acoustic stationary wave with same amplitude), that generates a periodic variation of the refractive index. The crystal will, therefore, act as an intensity modulated diffraction grating with frequency fm. The grating effect will add to the losses gained during propagation in the cavity, an additional periodic component at frequency fm.

If the beam impinges on the crystal in a direction parallel to the acoustic wave-front, the diffraction can be described by the Raman-Nath effect. Lateral bands symmetrically disposed with respect to the non-diffracted component will be generated after the grating. If the laser beam impinges on the crystal with an angle equal to ϑ_B (with respect to the acoustic wave-front),

$$\vartheta_B = srcsen\lambda_l/2n\lambda_s \qquad \textit{Eq. 10}$$

(where λ_l and λ_s are the wavelengths of the laser radiation and of the acoustic wave respectively) the diffraction is ruled by the Bragg effect, retrieving eventually a component that crosses the crystal without changing direction and another component of the beam that gets reflected at $\vartheta_r = \vartheta_B$. The stationary acoustic wave inside the crystal produces subsequent regions of high and low refractive index that work as partially reflective mirrors separated by distance λs. The Bragg incidence condition makes the laser beam reflected components (at each index discontinuity) interfere constructively, generating diffraction peaks.

In time domain measures it will be necessary to have a sharp temporal response, therefore a very short input excitation pulse. To have the sharper pulse as possible, we will look for the higher intensity modulation and the optimal frequency modulation that matches the crystal resonating frequency. To be considered though, that if the modulation intensity is too high the efficiency of the laser can drop significantly. It will be seen in the following paragraphs how parameter such as intensity modulation and incident angle on AOM can change the time and spectral profile of the outcoming laser pulses.

2.4 BRAGG ZONES - AOM

The power behavior of the outcoming beam versus the alignment angle of the acousto-optic modulator has been characterized. In that case, the output beam is pulsed with a frequency of 100 MHz. The crystal is mounted

over a system with two degrees of freedom on the vertical and horizontal angle. With a fixed horizontal angle the measurement has been taken by changing the vertical angle with constant variation steps. From the graph, we see that the efficiency of the mode locking on the laser changes with the angle position of the acoustic modulator, in particular, it presents a region of maximum efficiency, where the output power is lower. This region has got two minimum, called Bragg minimum and a maximum In-between. The angle where we have the local maxima is called Raman-Nath. In the two regions with local minima, we get the sharpest pulses in time that can be generated. The intensity of the output power can then further optimized by correcting the cavity length. Pulses with sharp time FWHM is a very important feature that has to be perused when it comes to time domain measures.

The measure of the output power vs angle tilt of the AOM has been taken with 2 different intensity of modulation of the frequency on the crystal, the results can be seen in *[Fig. 11]*.

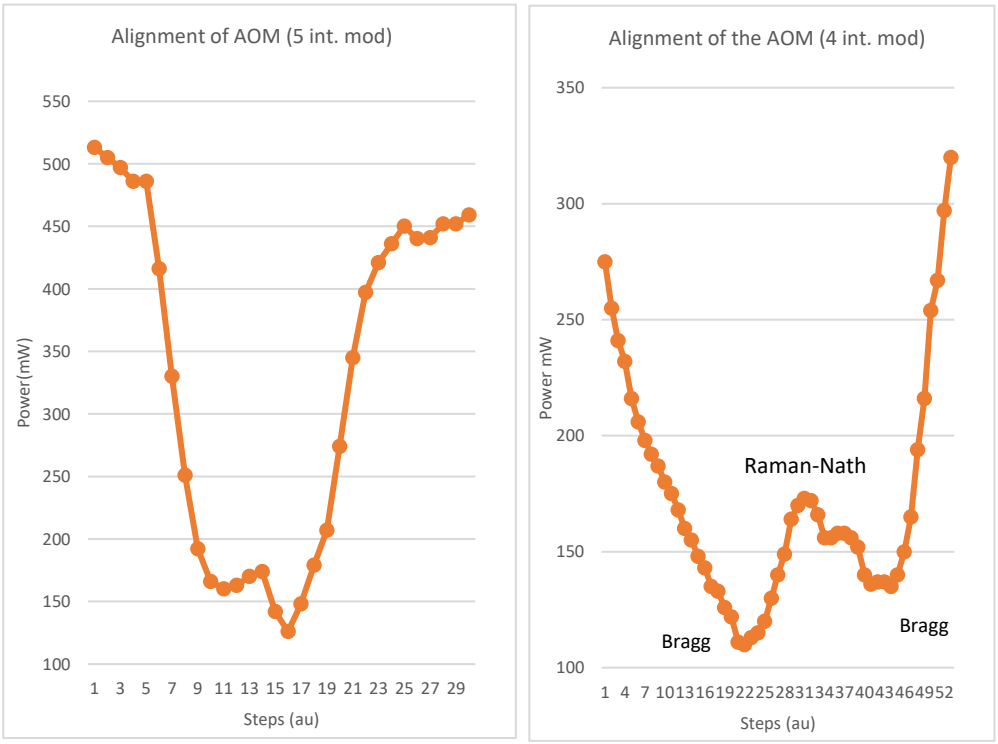

Fig. 11 Bragg regions, AOM alignment, the two figures corresponds to two different intensity modulations.

As we can see in the plots the curve behavior is strongly dependent on modulation intensity but it always presents the same general behavior of to local minima (Bragg zones) and a local maximum in the middle (Raman-Nath zone). In practice, before measures on samples, it will be needed to set the laser to its Bragg modes and optimize the cavity length to have maximum output power.

2.5 PULSE CHARACTERIZATION

By exploiting the features of a sensor made up by a chain of TCSPC, with sharper time resolution, 40 ps, compared to the Detector that will be implemented in the spectrometer *[section 3.5]*, it has been possible to see the effective time width of the pulses. Therefore the pulses have been characterized over the wavelength of the output laser emission. The measure has been made by aligning the cavity every time the wavelength was changed and keeping the same modulation intensity on the crystal. For each measure, the pulse width has been optimized trying to reach the minimum time width by changing the alignment of the AO crystal and optimizing the output power by moving the cavity mirrors. The pump power was set to constant power 4W and the intensity modulation was set constant as well at level 5.

In the following graph *[Fig. 12]* the FWHM of the laser in time has been measured versus the intensity of the modulation.

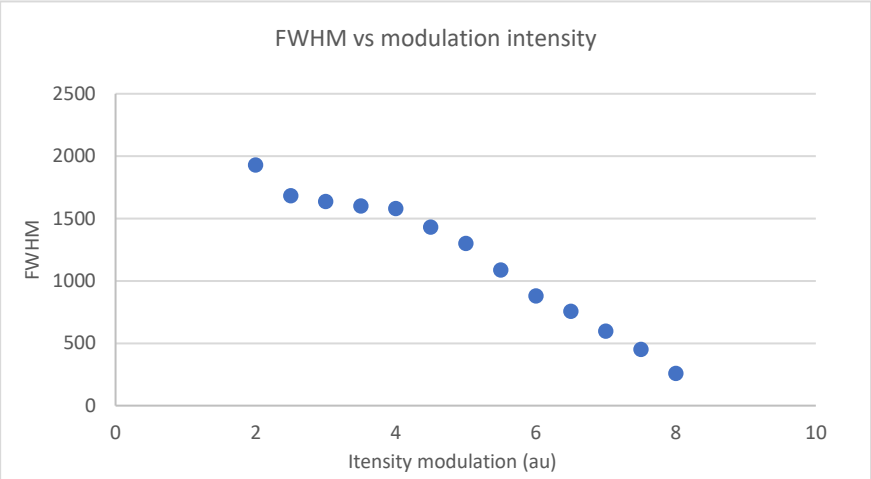

Fig. 12 FWHM in time vs Intensity modulation

The intensity modulation has been raised by constant intensity steps. The plot shows an increasing behavior of the sharpness of the pulse due to the increase in intensity modulation. The results for modulation intensities higher than 8 a.u. and lower than 2 a.u. are not shown due to the two main causes. If the modulation intensity is too low the laser goes out of the mode-locking mode and no pulses can be seen. On the other hand, if the modulation intensity is too high the losses are too intense and the stimulated emission does not occur.

2.6 SPECTRAL RESOLUTION

The spectral properties of the output laser emission have been calculated as the full width at half maximum of the spectrum of the laser beam collected by the *Ocean Optics spectrometer USB2000* with an optical resolution of approximately 0.1 nm FWHM. Laser emission wavelength was set to 785 nm. The spectra have been acquired firstly in CW mode *[Fig. 13a]* and later on, by switching on the radiofrequency generator in Mode Locking. For the second configuration, the optics have been optimized in order to reach the Bragg zone of the AO crystal and to have the sharper pulse in time *[Fig. 13b].*

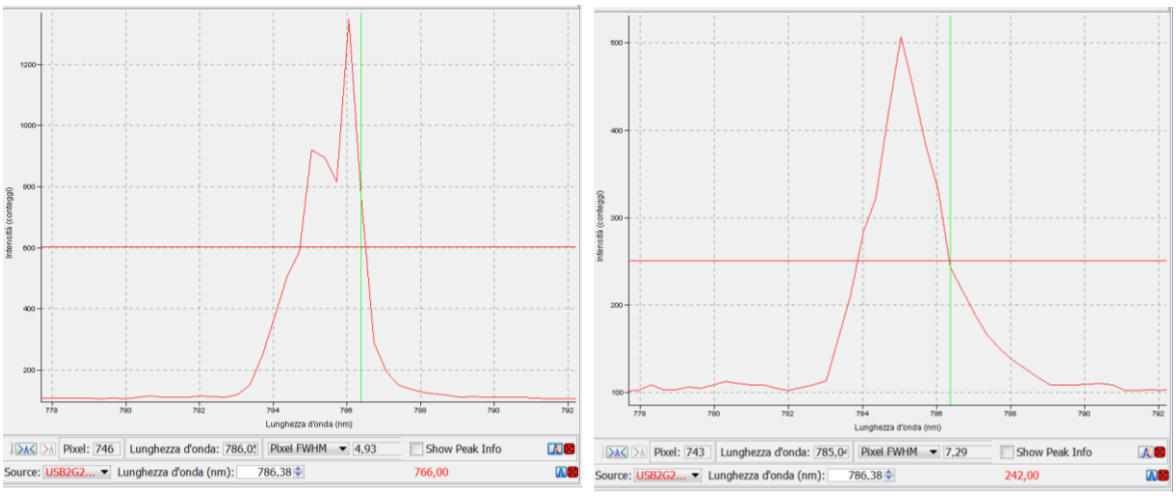

Fig. 13 a. on the left is shown the spectra in CW mode 2 nm FWHM. – b. on the right is shown the Modelocked laser spectra, 2.5 nm FWHM. In both cases the cavity length was set to 785 nm emission wavelength.

It is interesting to notice that there is a difference in the FWHM in the two cases. In CW configuration the FWHM is around 2 nm whereas in the Mode-Locked configuration the FWHM broadens but not significantly, it turns out to be around 2.5 nm. The center of gravity of the curve undergoes a spectral shift of 1.2 nm. The spectral broadening of the curve in modelocked mode was expected to be stronger due to the locking of a higher number of longitudinal modes. The weak broadening can be due to slight changes in the alignment when switching to mode-locking. One other reason can be that the mode-locking mode forces the laser to oscillate on a rigid gaussian spectral band whereas in CW band fluctuations are present.

2.7 IRF AND STABILITY

In order to better understand laser behaviors, studies on its stability in time have been made taking particular care to output power, the position of the pulse peak amplitude in time and FWHM in time. Stability is an important device feature when aiming at a system that can undertake repeatable measures on samples. It is needed to know how much time the laser can work on stable regimes providing pulses with same features, and how long

does it take to reach a stable regime after being turned on. In case of a big change in pulse features, it will reflect on drastic changes on the feature of the signal that can be revealed by a sample.

In the following set of measures, the Ti-Sa Laser has been set into modulated mode (100Mhz) and the pulse width has been optimized by looking for the Bragg zone related to the AOM angle tilt. Once the optimal tuning has been set, we have acquired Impulse Response Function (IRF) of the pulsed laser at 785 nm. The acquisition has been done with 10 second integration time for each curve and for a total period of 65 minutes. The temperature of the crystal was stable at around 18°C and the intensity modulation was set to a fixed value. Because of the long time needed to get the modulated mode of the laser working, the stability measure started after one thirty minutes from the starting of the pump.

From raw data the analysis has been focused on the power intensity of the outcoming beam, it's temporal Full Width at Half Maximum and the Center of Gravity of the peak. In the following pictures we can see the results of the analysis:

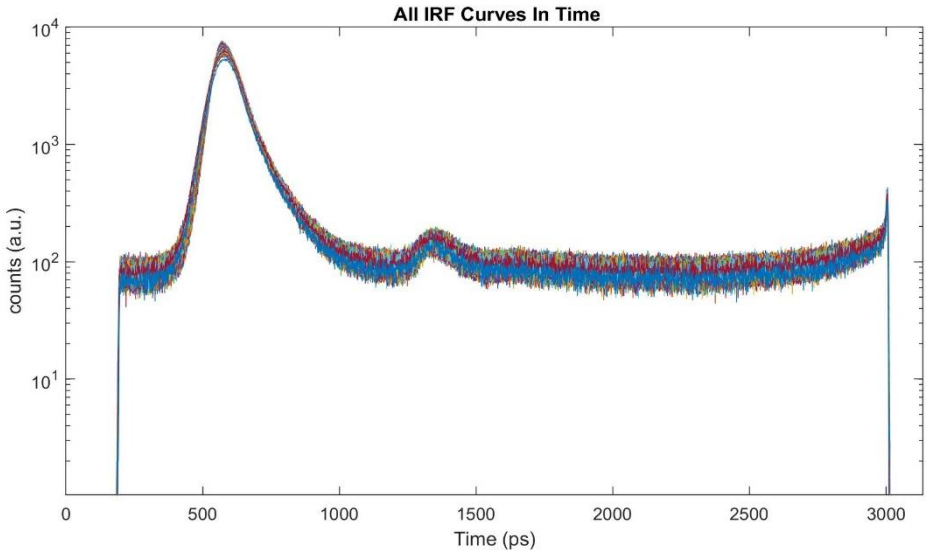

Fig. 14 All the 416 IRF curves superposed on the same graph, each curve is the result of 10 seconds integration time. Total measure time, 70 minutes.

In *[Fig. 14]* all the 416 IRF curves are superposed, each one resulting from 10 seconds of integration time. The 10 seconds of integration time has been

acquired in sequence for a total time measure of 70 minutes. The curves in semilogarithmic scale, show a main pack due to direct laser emission and a small reflection at approximately 1 ns distance. It is also noticeable a second small peak at nearly one ns time distance from the main one, it is probably due to some reflections of the laser beam inside the system. This is a typical time fingerprint of the laser pulse.

From the measure of the mean integrated counts per each curve in time, in *[Fig. 15]* it is possible to notice that the output power of the laser is relatively stable along all the measured time. The number of counts detected, is a fair indicator of the output power, given that the wavelength and the width of the pulse are fixed. The dashed curves show the 10% deviation in number of counts from the mean value. It is possible to appreciate, the maximum deviation is well below the 10% value for all the time of measure. The maximum oscillation away from the mean value is of 6 %.

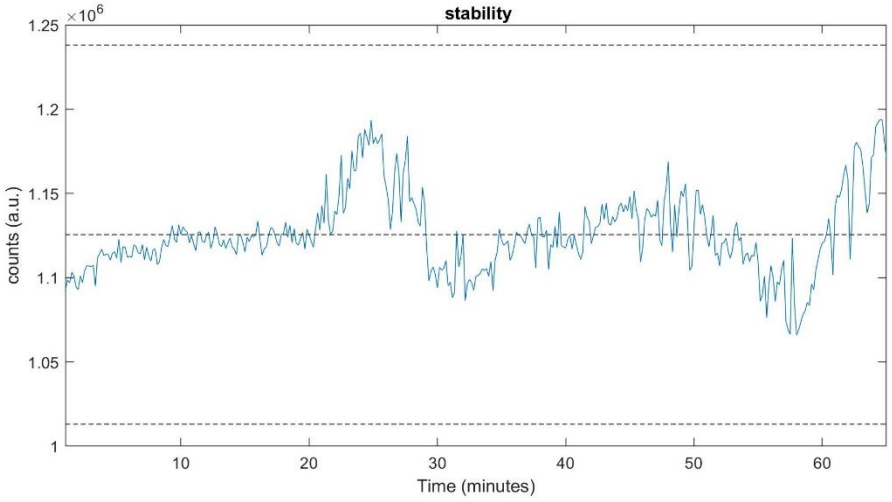

Fig. 15 Number of counts, integrated over 10 secodns during all the measured time. Dashed lines rapresent the 10% deviation trashold. Mean value 1.13x106 counts a.u.

The FWHM *[Fig. 16a]* of the pulse shows an increasing behavior in time, that can be considered linear in the first hour period. Starting from 90 ns time width and ending up with a value of approximately 117ns.

On the other end, the Center of gravity *[*Fig. 16*b]* shows a very slight increase during the one hour measure. Starting from the time position of 573 ns and

finishing with 581 ns time position. The total effective shift of the center of gravity in time is less than 6 ps. Such a shift is acceptable in diffuse optics because it comes out to be a lot shorter than the usual temporal dynamics that are around hundreds of ps or even on ns scale.

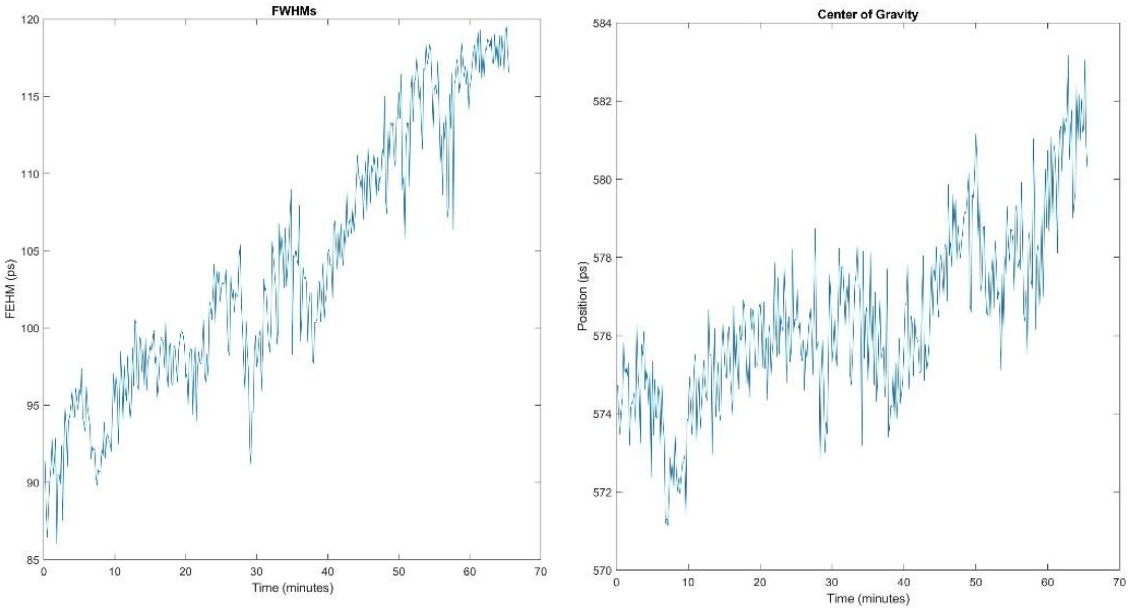

Fig. 16 a) FWHM in time b)Center of Gravity over time

2.8 CRITICALITIES OF THE LASER SYSTEM

In this particular system, the stability of oscillating mode-locked waves inside the cavity is as important as it is hard to achieve. As we can see in *[Fig. 16a]* from the previous paragraph the pulse FWHM changes significantly over one hour time even if the temperature of the active crystal and frequency modulation are kept constant. In particular, the active material is surrounded by an aluminum case in which passes a constant flow of cold water at 18°C. The instability of the modes oscillating inside the cavity has not been deeply studied but it is probably due to very small changes in mirror positions and relative distances probably due to thermal variation. The element inside the laser cavity that is the most crucial for the whole

alignment is probably the spherical mirror that focusses the beam on to the face of the rod.

Power stability in mode locking is also not easy to achieve, it mainly depends on how the laser has been turned on and on the stability of the pump. In fact, the turning on process of the laser is crucial to its stability and output power. The laser pump must be very stable and it's temperature at around 18°C. Its power must be gently raised from 0.22W to 4W in a time window of approximately 5 minutes in order to avoid abrupt changes in temperature on the active material that must be chilled at a stable temperature of 18°C. The stability of the pump laser is a less critical variable given that it is a commercial laser and it is supposed to be sufficiently stable. One other critical device is the generator of radiofrequency since it is more than 30 years old, it can probably be a source of oscillating behaviors and modes instability inside the cavity. If the frequency modulation on the AO crystal drifts than also the looking of the modes changes and it can bring to a broadening in time of the FWHM.

3 CHAPTER 3 – DEVELOPMENT OF THE TIME DOMAIN RAMAN SPECTROMETER

3.1 CONCEPT AND RATIONAL REQUIREMENTS

The need for a compact, cheap and fast device to fully exploit the potential of time-domain diffuse Raman analysis is strong, and it becomes more important every day. Innovative solutions have raised making devices faster and more affordable. Compressive sensing, with the use of spatial light modulators (SLM), has been the center of the upgrades mentioned above. This project will be based on the implementation of compressive sensing in a Raman spectrometer eventually applied in measures for diffuse media. The spectrometer analysis will be carried out in the domain of time, thanks to the modelocked laser and the SPC detector. Compressive sensing and time domain diffused Raman spectroscopy merged together have not been presented in the literature yet.

The knowledge acquired from important projects undertaken in the Department of Applied Physics of Politecnico di Milano, treating specifically time domain compressive sensing tomography with SLM [49] and design of time-domain diffuse Raman spectrometer for depth probing of highly scattering media [26], will give some guidelines to the development of this new project.

A new Time Domain Compressive Diffuse Raman Instrumentation based on a single pixel detector for depth analysis of diffusive media will be designed, constructed and tasted. Reaching a full working device that can be coupled to different kind of probes, microprobes and diffusive probes *[Appendix]*. The Instrumentation will be completely built in our labs and will come out as a

cheap device compared with CW Raman instrumentations commercially available.

In the following chapters, the reader will be brought step by step through the design, characterization, and optimization of the device.

3.2 SPECTROMETER DESIGN

I present here the full picture of the Time Domain Compressive Raman Spectrometer (TDCRS).

The Raman signal will be collected from the probe through optical fibers and will enter the spectrometer in position A *[Fig. 17]*. The Raman light beam will be then collimated with a collimation lens, guided through a transmission diffraction grating and focused on plane B by a second lens. On plane B the SLM will be present that in our case has been chosen to be a Digital Micromirror Device (DMD) provided by Texas Instruments. This first optical branch will be named as "collimation and focusing on DMD" and it will be presented in section *[3.3]*. The second branch is dedicated to collimation and focusing of the spatially modulated signal on to the Detector active area and it will be described in section *[3.4]*. During the development of the system, two different optical layouts have been tested configuration_1 and configuration_2. The main differences are the optical planes on which the beam is transmitted and the f-number of the system that switches from f/4 to f/2. The f-number has been calculated as the ratio between the focal length of the lenses and the lenses diameter. The system in both configurations will eventually lead to a 1:1 image system to the B plane on the DMD.

3.2.1 Configuration_1 :

In the first configuration, the f/4 layout has been exploited. Willing to keep the device as small as possible, 25mm diameter components have been chosen. A 300 line per mm transmission grating has been used to diffract

light. Therefore the collimated beam has been spatially limited by an optical iris to make it fit on the grating surface. Lenses with 25mm of diameter have been then used for the rest of the setup. The DMD position was set to reflect the beam on a tilted plane, in fact, the detector position came out to be not parallel to the optical table surface. The iris in the first branch is transforming the f-number of the system from f/2 to f/4. The setup layout can be seen in *[Fig. 17].*

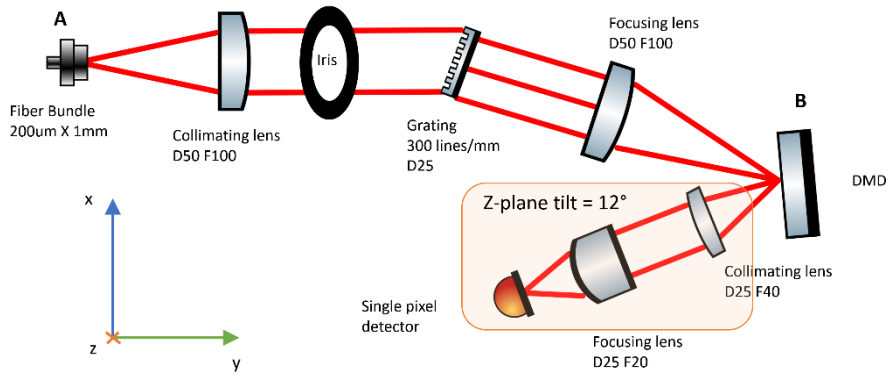

Fig. 17 Config_1 : The collimating and focusing branch on the detector is tilted from the optical plane parallel to the optical table surface. The resulting system is a f/4 system.

This has been the first configuration and the one used for most of the characterizations tests. Pictures of the completed optical layout can be seen in *[Fig. 18].* Due to efficiency problems and difficulty on the alignment of the second optical branch a second configuration has been designed and implemented.

Fig. 18 Configuration_1 optical setup, in both figure the input beam from the fiber bundle is coming from the bottom of the picture, the first lens works as collimator D50 F100. Follows the aperture and the grating (squared optical elements). After the grating the beam is focused on the DMD (The red element is the DMD electric board) . once the beam is reflected from the DMD in on state it enters the second branch, made up by the two lenses D25 placed on a different propagation plane, together with the Detector cage.

3.2.2 Configuration_2:

The second configuration is characterized by an f/2 lenses set up. Thanks to the removal of the optical iris, the intensity of the signal have been raised by a factor of four. A better optical design has been studied in order to keep the second branch of the spectrometer, the most critical branch in terms of alignment, on the optical plane parallel to the optical table surface. Due to this design choice, the input signal from the fiber has to come into the spectrometer at an angle that has to match to the diffraction angle of the

optical grating. Therefore the first collimation branch is set on a plane that is tilted from the parallel to the optical plane. The second configuration can be seen in *[Fig. 19]*

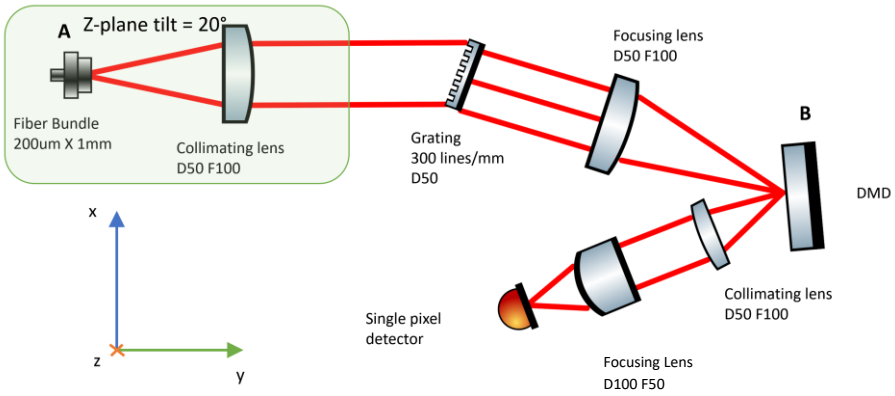

Fig. 19 Config_2: the collimating branch on the grating is tilted from the optical plane parallel to the optical table surface. The resulting system is an f/2 system, the iris has been removed.

In the following pictures *[Fig. 20]* it is possible to see the Configuration_2 optical setup. Photos have been taken directly on the optical table in the laboratory, before the system enclosed in a black box.

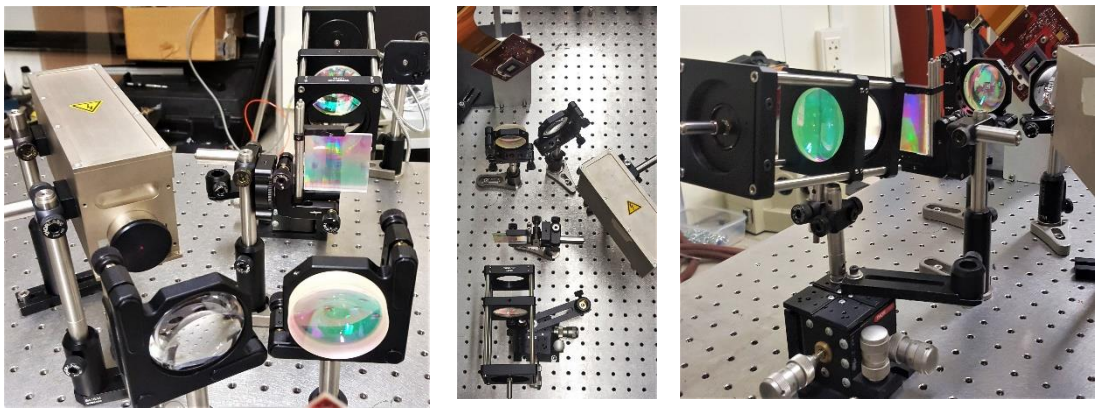

Fig. 20 Configuration_2 optical setup. From the figure in the center (top view) it is possible to see the complete setup, the input signal is coming from fiber tip that can be seen in the bottom of the picture in the middle. In the picture on the right the first branch is clearly visible, and it is possible to notice how the optical plane of the first branch is tilted with respect to the table surface. As it is possible to notice in the picture on the left (point of view from the DMD) the detector and the second branch are placed on the plane parallel to the table surface. Making alignment easier.

3.3 COLLIMATION AND FOCUSING ON DMD

This section will walk the reader through the design of the first branch of the spectrometer, including collimation after the fiber bundle, diffraction due to grating features and focusing on the Digital light modulator device. It is important to notice that the final set up was born after various trials and simulations. The most important aim in this section was to end up with the best spot (1:1 image of the fiber bundle tip) on the DMD plane. Only some of the trials will be shown here and the reason why lenses instead of mirrors have been chosen will be explained. Decisions on the optical layout will be justified with simulation made on Zemax software.

3.3.1 Zemax simulations

For the design of the spectrometer branches, Zemax simulations have been executed with optical elements as similar as possible to the ones used in practice. In particular, in *[Fig. 21]* it is possible to see the ray tracing layout for the first branch, collimation and focusing on DMD. As system parameters, the wavelengths 700, 750, 800,860 nm have been used, for an f/4 system (focal length: 100 mm, D= 25 mm) with 300line/mm Grating, The fiber bundle has been represented ad a rectangular slit object with major dimension 1mm and lower dimension 0.2mm.

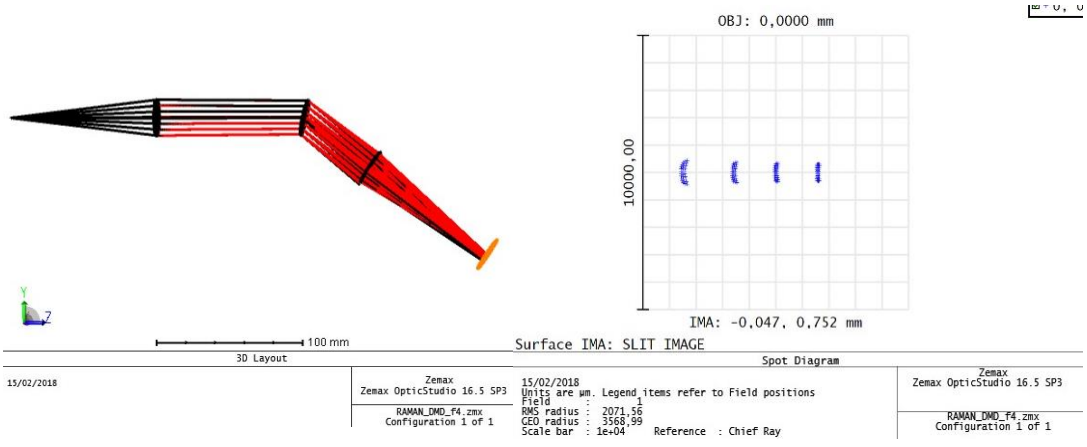

The dispersion width on the focal plane on DMD came out to be as much as 5 mm length. Considering that the active area of the DMD is 16.25 mm x 5 mm size it will be exploited the higher dimension to cover all the dispersion width. Note that the dispersion width for a $\Delta\lambda$ = 160 nm is 5 mm than it is possible to predict that we will be able to cover with the DMD active area a total range of approximately 480 nm. This also gives a great margin for future improvement on spectrometer resolution. In fact, if the line density

Fig. 21 Zemax simulations of the collimation and focusing on DMD plane. On the left, the raytracing layout from left (finger bundle tip) to right DMD plane in orange. On the right, the image of the fiber bundle tip for different colors.

of the grating will be increased, it will be possible to have a greater dispersion width, therefore more resolution on the selectivity of the wanted wavelength, the wavelength range covered by one single pixel of the DMD will be smaller.

3.3.2 Digital light modulation with Digital Micromirror Device

The Digital Light modulator used in this project has been provided by Texas instrument and it is the DLP LightCrafter 6500 evaluation module [50] *[Fig.* 22*]*. At the heart of DLP LightCrafter, 6500 is a DLP chipset comprising of: DLP6500FYE - Digital Micro-mirror Device (DMD) and DLPC900 - DMD digital controller. The DLP6500FYE has HD resolution, 1920 x 1080, 2 million programmable micromirrors, with an effective active area of 16.25mm x 5mm. It can be used to produce high-speed patterns using the DLPC900, up to 9,523 Hz binary pattern rate and up to 247 Hz 8-bit grayscale pattern rate. This device has been controlled either with the factory software provided by TI or a homemade MATLAB code.

Fig. 22 Texas Instrument http://www.ti.com/tool/DLPLCR6500EVM

DMD has good reflecting efficiency from 400 to 700 nm [51], in this project it is going to be used on the tail of high-efficiency window.

The DMD will be used firstly as a sharp slit spatial filter in reflection mode, it will reflect only the wavelength that has been ubicated in pre-selected positions thanks to the dispersion of the grating. Secondly, when the CS will be implemented into the system, it will work as a compressive sensing pattern creator. The micromirrors composing the devices have a pixel pitch of 7.56 µm and only the on and off position of the pixel have been exploited. Micromirrors, in fact, have 24 degrees of maximum tilt on the diagonal of theirs squared shape. On position will reflect light at +12 degrees from the normal and off position at -12 degrees from the normal of the pixel surface. The zero states will be the one corresponding to zero degrees tilt from the normal. Note that, the pixels tilt on their diagonal, therefore light coming on a plane perpendicular to the zero state surface and parallel to the optical table plane, will be reflected on a plane tilted of 45° from the table surface and 12° from the normal of the pixel surface. This is the case of Configuration_1, where the detector has a tilt of 45 degrees from the table surface. Whereas in Configuration_2 the DMD have been rotated 45° on its normal axis in order to have incident and reflected beam on the same plane parallel to the optical table surface.

Set up design has been inspired by similar projects that exploited DMD features in Raman Spectroscopy systems such as ref [44] and ref [46]. In those two cases, DMDs have been used either to enable programmable

spectroscopy acquisition for Raman scattering microscopes or for generic compressive spectral imaging.

3.3.3 Fiber bundle

The fiber bundles used to guide the light beam at the entrance of the spectrometer has been provided by Thorlabs. It contains seven 200 µm Core Multimode Fibers arranged in a line configuration (linear) at both ends *[Fig. 23]*.

Fig. 23 tip of the fiber bundle
https://www.thorlabs.com/newgrouppage9.cfm?objectgroup_id=8279

Linear-to-linear fiber bundle cables are ideal for increasing the coupling efficiency into spectrometers and other optical devices that have an entrance slit. The linear ends match the shape of the entrance slit better than a single fiber or round bundle configuration and therefore increase the amount of light entering the device. It has been chosen to use this fiber in order to have as much signal as possible exploiting the large dimension of the fiber on the plane perpendicular to the dispersion plane of the grating. In this configuration, the maximum spectral resolution will be related to the

lower dimension of the fiber bundle together with the DMD pixel dimension and the dispersion power of the grating. The smaller the fiber bundle, the smaller the dimension of the focused spot on the DMD, therefore, the higher the spectral resolution. All the above assumptions can be made given that the pixel width is significantly smaller than the laser spot, in our case 7.56 µm pixel dimension versus 200 µm spot dimension.

3.3.4 spot on DMD

Given that the system is a 1:1 image system, the spot generated on the DMD plane from short bandwidth laser pulse (3, 4 nm) will be, if the optics are mounted properly, a linear disposition of seven 200 um fibers placed one over the other. The image of the fiber bundle on the DMD plane can be appreciated in *[Fig.* 24*]*.

Fig. 24 Focused beam at 785nm on DMD plane, acquired with Newport camera. Lower dimension 200um , higher dimension 1.3mm. Small circular fiber, radius 100um approximately.

It has been possible to make those measurements thanks to the spectrally sharp laser beam that can be produced by the Ti-Sa laser. Thanks to the laser tunability It has been possible to check the quality of the image spot for different wavelength, from 700 nm until 860 nm.

The images have been acquired through a beam profiler commercialized by Newport: (LBP2 Series Laser Beam Profiler).

From the above image, it can be appreciated that all the fibers that build up the fiber bundle are replicated on the image plane and that the spot is well

focused free of aberration. To be able to couple all the fibers of the bundle, the laser light coming out from the Ti-Sa laser have been first coupled to a 400 um core fiber and then to the fiber bundle. A thin piece of Teflon has been inserted as diffusor between the two fiber tips in order to diffuse the light coming out of the 400um fiber on all the fibers of the fiber bundle. As it is possible to appreciate from *[Fig.* 24*],* some fibers of the bundle receive more light intensity generating brighter image spots. It means that the coupling with all the fibers is not perfectly homogeneous, but it will not be a problem for our applications.

By tuning the laser it has been possible to experimentally characterize the dispersion width from 700 nm to 860 nm (details on the measure can be seen in the next chapter *[4]*). Results came out to be in accordance with the simulations, with a total dispersion width of 5.2 mm.

In *[Fig.* 25*]* is reported a sketch of the position of the spot (red slit) of a monochromatic beam on the DMD active area to give a better idea of the image plane. In different color (light blue) is depicted also the area occupied by a wavelength range of 160 nm, DMD active area is represented with a light red rectangle.

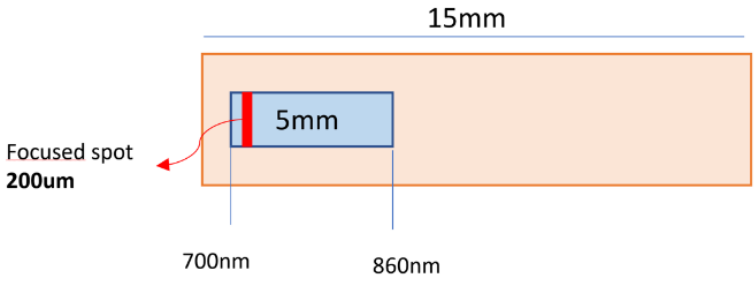

Fig. 25 Sketch of the image plane on DMD. Orange area: DMD active area. Blue: total area covered by light dispersion. Red Slit: slit image on DMD plane.

3.3.5 Aberrations

Aberrations are crucial for the spectrometer spectral resolution. If the image is affected by aberration, cross-talk between near wavelength can happen and the effective spectral resolution can be lowered significantly. Due to the dispersion of the grating, different wavelengths come into different position on the focusing lens. Because of this phenomenon, coma aberration can be present on the images when the wavelength entering the system is far apart from the one used to optimize the optical layout.

As a first system design, the optical layout of the first branch included a 50 mm diameter spherical mirror with a 100 mm focal length. The image spot at the best alignment it was possible to achieve is shown in *[Fig.* 26*_left side].*

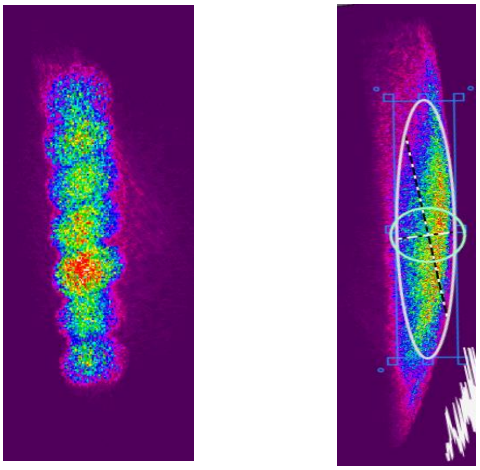

Fig. 26 on the left: spot on image plane of the fiber bundle with laser beam at wavelength 785nm, to be compared with [Fig. 242] on the right same optical configuration but wavelength 860nm

As it can be appreciated, the image of the fiber bundle achieved with mirrors is not as good as the one achieved later on with focusing throughout the lens *[Fig. 24]*. It can be noticed also that the system is very sensitive to aberration when the input laser wavelength is tuned. Therefore due to the poor image capability of the mirror layout and its increasing level on layout complexity (due to reflection properties of the mirror, and light path folding) it has been choose to follow the system construction by exploiting a focusing lens with 50 mm diameter an 100 mm focal length, same as the collimating lens. Above picture on the left side presents a spot with lower dimension

400 um and higher dimension 1.9 mm and on the right side 600 um x 2 mm (the two pictures are not in the same scale system). Those results have to be compared to the results shown in *[Fig. 24]*.

Also with the lens set up, the main challenge was to achieve a good image for every wavelength. But it brought to significantly better results compared to the mirror setup. A trade-off must be therefore applied in order to have acceptable images on the focus plane for all the wavelengths. Knowing that the samples will be exited with 785 nm pulsed laser beam, the Raman signal that will be relevant in our measure will always have wavelengths higher than 785 nm (Stoke Raman Shift). Therefore the optimization of the image spot will be performed at 800 nm, and by tuning the laser at lower frequencies will be then optimized. An image sequence of all the focused spot at a different wavelength can be seen in *[Fig. 27]*.

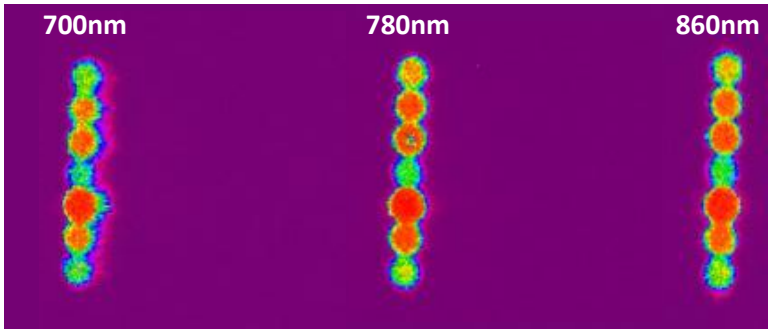

Fig. 27 focused images of the fiber bundle at different input wavelength on the DMD plane spots diameters : 205 µm

It is possible to appreciate good image spots at all wavelengths. It can be noticed a slight aberration, probably due to Coma at 700um. The aberration contribution was characterized by an increasing behavior from 740 nm to 700 nm, it can further confirm the fact that it is probably due to an increasing spatial shift of the beam from the center of the focusing lens, due to grating dispersion. The slight tilt of the bundle is due to a wrong positioning of the fiber bundle at the entrance of the spectrometer. When performing measurements the positioning of the fiber tip will be very important, the less vertical it will be, the more crosstalk will result between neighbors wavelengths.

3.3.6 DMD tilt

Due to optical set up constraints the DMD had to be tilted because 24 degrees of maximum tilt of the pixels were not enough to place the off position of the beam outside of the focusing lenses area occupied by the second branch layout. To be sure that the tilt of the DMD would have not worsened the image spot, an optical set up for testing the influence of the DMD tilt has been assembled, as shown in *[Fig. 28]*.

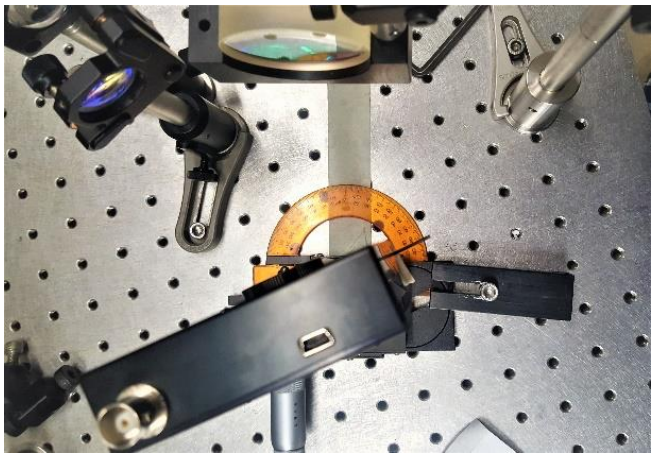

Fig. 28 Setup used to test the influence of the DMD tilt.

Measures have been taken on the spot positions and spot dimension related to the constant step of angle tilt of the DMD. by applying a tilt on the DMD active area, its projection on the plane perpendicular to beam propagation reduces, decreasing the maximum wavelength range that can impinge on DMD mirrors. The DMD tilt will then reduce the maximum Δλ that can be analyzed from our spectrometer. Graphs showing the effect of the tilt on the variables that have been pointed out can be seen below *[Fig. 29,*

Fig. 30*,* Fig. 31*].*

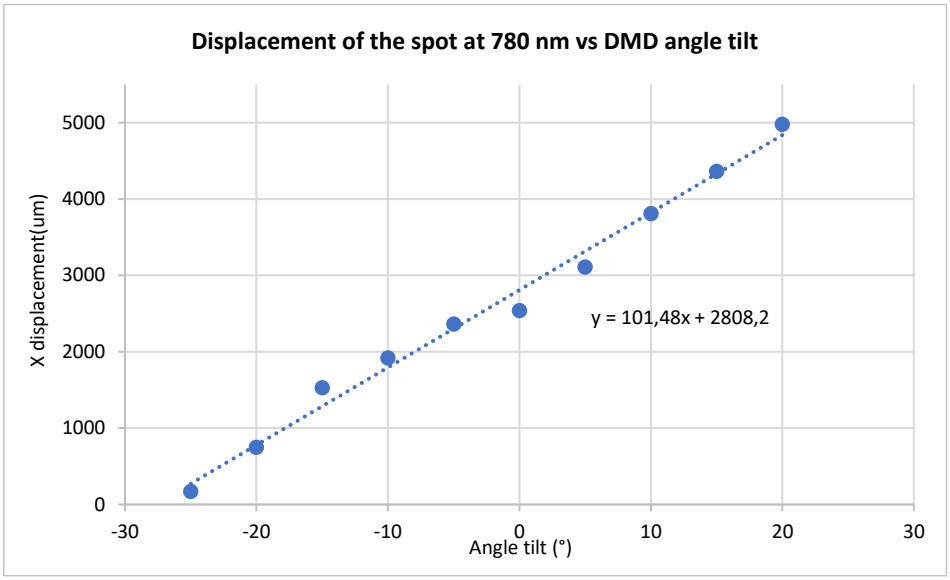

Fig. 29 Displacement of the laser spot on DMD plane related to DMD tilt.

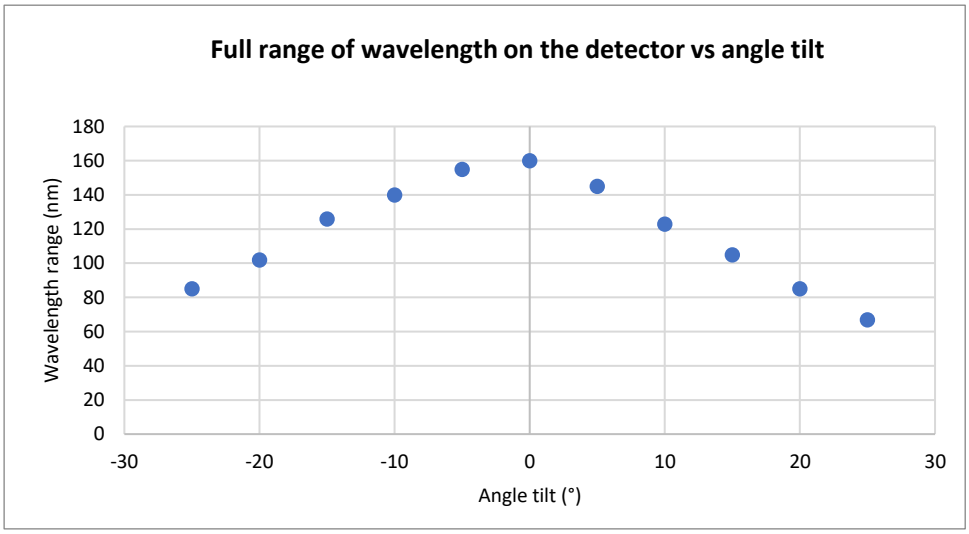

Fig. 30 Wavelength range that can fit in the DMD active area versus DMD angle tilt.

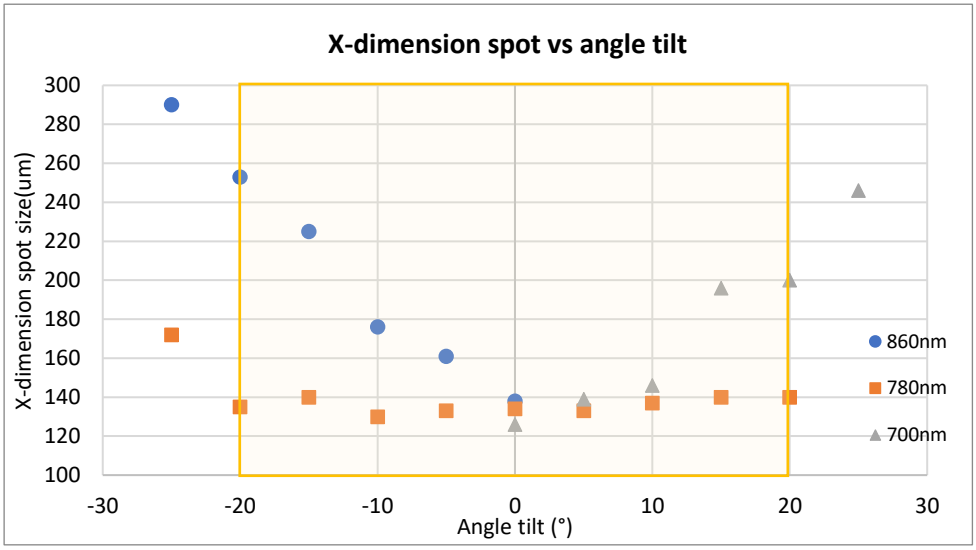

Fig. 31 Spotsize of the fiber bundle image on the DMD vs DMD angle tilt. The same measurement has been done at different wavelengths.

In *[Fig. 29]* it can be seen that the displacement of the spot position on the DMD plane is nearly linear with the angle tilt variation. By tilting the DMD, the light path varies and the beam impinges in different DMD positions. This leads to a different calibration of the system for each angle tilt and the possibility to have out of focus images if the tilt gives significant path difference.

The graph in *[Fig. 30]* reveals that the maximum wavelength range that can fit in the DMD active area decreases linearly with variation in absolute value of the DMD angle tilt. In fact, the effective active area can be seen as the projection of the DMD surface on the plane perpendicular to the optical axis. The more the DMD is tilted, the less surface will be occupied by its projection, therefore less effective active area will be available.

In *[Fig. 31]* the variation of the spot size, in its lower dimension, vs angle tilt is shown at three different wavelengths. The change in the spot dimension for the 780 nm wavelength is nearly zero, while it increases in different tilt directions for the wavelengths at the edges of the $\Delta\lambda$ of interest. The strong dependence of the spot dimension over the angle tilt is probably due to the presence of stronger aberrations for wavelengths at the edge of the working spectra. If 860 and 700 nm wavelengths are ubicated on the sides of the

DMD active area, the path difference will be stronger when the DMD is tilted and the DMD plane can shift far apart from the focal plane. The dependence on only one direction of the tilt happens because, in the other direction, the external wavelength spot falls out of the DMD active area. Spot dimension in *[Fig. 31]* comes out to be less than 200 um, and it could result quite strange, given that the fiber bundle has an x dimension of 200um. It can be due to the fact that the value of the x dimension is taken as FWHM of the intensity of the spot and it can be lower than the real object dimension. On the other hand, a smaller spot can be generated in case of the wrong positioning of the collimating lens after the fiber bundle. In fact, if the collimating lens is ubicated further apart than its focal length, the "collimated beam" can have a slight focusing behavior that can increase the apparent focal power of the focusing lens ubicated just before the DMD and after the grating

By analyzing the graphs, from the tilt of the camera, it has been possible to set a maximum angle over which the gained aberration would not have compromised to much the image spot. As a result, the spot was acceptable at all the wavelength till a maximum angle around the axis perpendicular to the optical plane of 25°. Considering that our set up needs a tilt of 17 °, there will be no significant changes connected to the DMD tilt.

In *[Fig. 32]* it is possible to notice the effect of the tilt on the focused spot at the image plane. The data were acquired with the Newport beam profiler. Stranger light intensity is shown in red color and weaker intensity in blue.

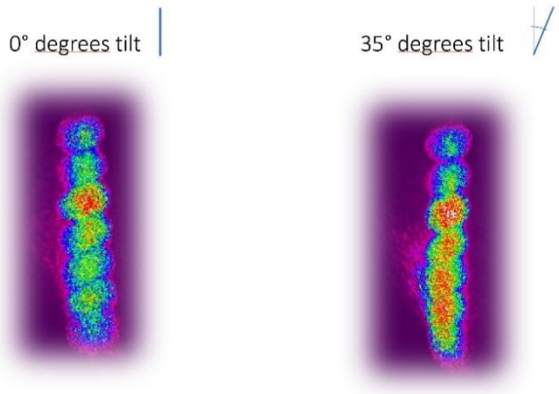

The beam profile at 785 nm on the image plane on the DMD looks sufficiently defined even at 35° tilt, left side in *[Fig. 32].* Considering that, to have the DMD off position out of the second optical branch (focusing on the detector) we only need 17° tilt, we are now confident that the tilt will not affect significantly the spot position and shape.

Fig. 32 Laser beam profile at the image plane on the DMD at two different DMD algle tilt.

3.4 FOCUSING SYSTEM

The following chapter is dedicated to the description of the second optical branch of the spectrometer. The first part will describe and justify the design of the set up focusing the light reflected from the DMD (in on state) onto the detector active area. The second part will focus on the description of the detector in use and on the amplitude dynamics of the system.

3.4.1 Zemax simulations

Simulations have been conducted also on the second branch of the spectrometer. After the focus on the DMD plane, light is reflected, and passing through a focusing system a new rescaled image of the fiber tip impinges on the detector active area (radius of 3mm). The last focusing system is made of one single lens in the simulation, in practice, we have noticed later on that the coupling of a collimating and a focusing lens improves the image quality and focusing power on the detector plane.

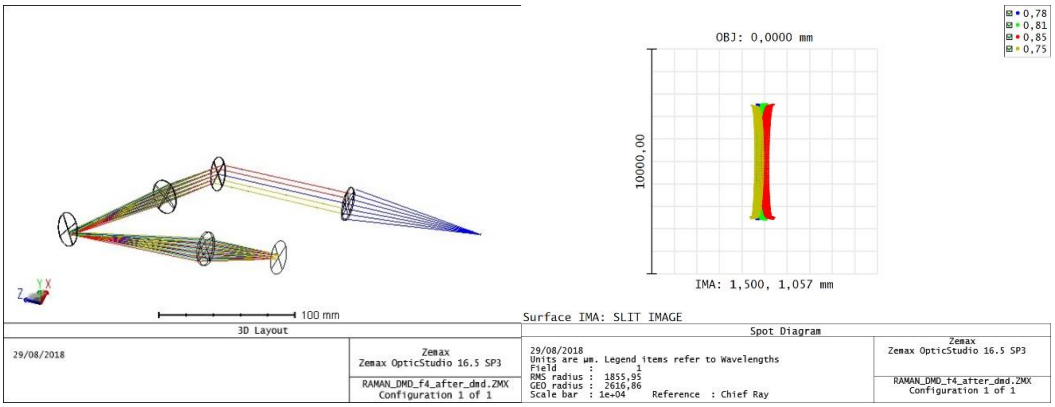

Fig. 33 On the left, raytracing simulation of the whole optical layout, surce is ubicated at the beginning of the blue raytracing pattern. On the right focused spot (imaged of fiber bundle tip) at different wavelengths750 nm (yellow), 780 nm(blue), 810 nm (green) 850 nm (red).

All the light that has been diffracted from the grating is now focused into the active area of the detector. In *[Fig. 33]* it is possible to see that all the image spots are nearly superposed on the focal plane. This is a very good result, meaning that spectral information, even if far apart in wavelength is focused at the same position and only one small area detector will be needed to retrieve all the information. In *[Fig. 33]* is shown that a spectral bandwidth of 160 nm has been focused on an x-dimension of less than 2 mm (1.2 mm exactly). It means that all the wavelengths can be retrieved by the 3 mm radius active area of the detector, without any loss of information.

3.4.2 Design and optimization

Reflected light from DMD has to be guided to a collimation and focusing system that will produce a sub scaled version of the image on the detector active area. The active area of the detector here used is a disc with 3 mm diameter. The image of the dispersion of the wanted wavelength range (160 nm) that occupied 5 mm width on the DMD active area must then be confined into maximum 3 mm dimension width. To be able to reach this

specification, the lens set up used in *[Fig. 17]* have been eventually adopted after a series of trials sowed in *[Fig. 34]*

	ΔX (mm)	Spot Xdiameter (um)	Angle from NA
1. Collimator D25 F40 – Focus D25 F20	1,5	442	12,3
2. Collimator D50 F60 – Focus D25 F40	2,1	507	18,9
3. Collimator D50 F60 – Focus D25 F20	4,0	661	6,9

Fig. 34 Table showing the performances of the 3 different optical set up proposed for the second section of the spectrometer in the case of Configuration_1.

The measures have been taken with the Newport camera, in the above table are shown the values of the total dispersion width (ΔX) from 700 nm to 860 nm, the focused spot diameter and the numerical aperture of the light beam impinging on the detector. Measures have been taken using a 1 mm core fiber as input to the spectrometer. As we can see the optical layout n.1 is the one that presents the best performances, giving the possibility to exploit only half of the active area diameter of the detector for a 160 nm spectrum scan. Comparing the dispersion width on the detector plane with the one on the DMD plane it can be retrieved that a rescaling of nearly 2/7 has been achieved. In this second section of the spectrometer, device aberrations do not play such a critical role as in the first section. Given that the detector is a single pixel camera. All the spectral information given at a certain time, are integrated on the active area of the single pixel. Crosstalk between neighbors wavelength is not important because the information is integrated, whereas it is of main importance having no loss of information. In other words, the full spectral image must fall on to the detector area without any loss on the band edges of the Δλ of interest.

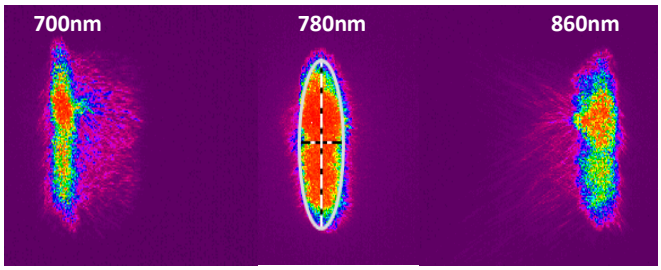

Fig. 35 focal plane on the detector single pixel. Stonger aberrations can be seen compared to the case of focusing on DMD plane.

In *[Fig. 35]* it is possible to appreciate the focal spot of the fiber bundle tip on the detector position. The laser has been tuned from 700 nm to 860 nm in steps of 10 nm and the image of the spot have been analyzed. The diameter of the lower spots dimension was always beneath 200 um and the total dispersion width is 1.5 mm.

Aberrations on the focused image are stronger compared to the ones seen on the DMD plane and are still mainly related to coma, due to the position of the beam impinging on the focusing lens. With the system optimized at 785 nm, light beams of a wavelength close to the band edges will fall far away from the center of the focusing lens. Therefore gaining aberration that will broaden the effective focal image towards the direction opposite to the space shift from the center of the lens.

3.5 DETECTOR

The detector is a Hybrid Single pixel avalanche photodiode active area of diameter 3 mm. The High-Speed Hybrid Detector for TCSPC (Time-correlated Single Photon Counting) is provided by “Becker & Hickl GmbH”. HPM-100-50 module *[Fig. 36 top right]* combines a Hamamatsu R10467-50 GaAs hybrid detector tube with the preamplifier and the generators for the tube operating voltages. The principle of the hybrid detector in combination with

the GaAs cathode yields good timing resolution and high detection quantum efficiency up to NIR wavelengths (900 nm). The TCSPC instrument response function can be seen in *[Fig. 36, red curve]* with an FWHM of 130 ps. The after pulsing of the module is very low, tending to an increased dynamic range of TCSPC measurements.

It has been preferred between others because of its high dynamic range, high quantum efficiency even in near-infrared region and very low afterpulsing probability.

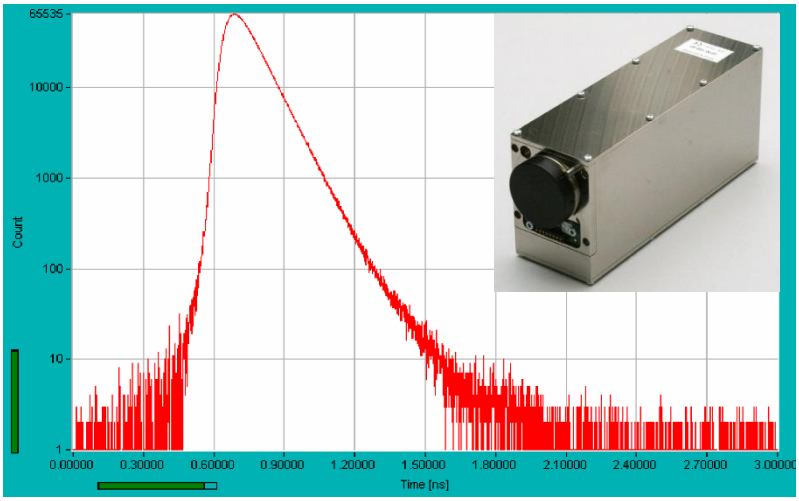

Fig. 36 TCSPC IRF of the hybrid detector in logarithmic scale FWHM 130ps, taken from https://www.becker-hickl.com/pdf/dbhpm-50-04.pdf . On top right corner, the detector itself

The aligning of the detector is crucial especially in Configuration_1, due to the inclination of the optical axis. By measuring the light intensity retrieved in the on and off state at the detector active area we managed to see the contribution of the unwanted signal. The unwanted signal is the light that the SPAD will measure when the laser is pulsing but the DMD is in its off state (not reflecting on the detector but 24 degrees away) also called straight light. It has been measured the amount of stray light vs the intensity of the signal (detected light in on and off position of the DMD mirrors). As it is sown in *[Fig. 37]* there are approximately three decades between the two signals. This can demonstrate that the DMD sufficiently drives the light away from the detector area when off status is needed. It is very important to avoid background noise and straight light coming into the system. This is the

reason why it has been created a box for the spectrometer in order to avoid diffused light from outside, and we also built an insulating light protection for the focusing system to avoid free laser light diffusion into the detector.

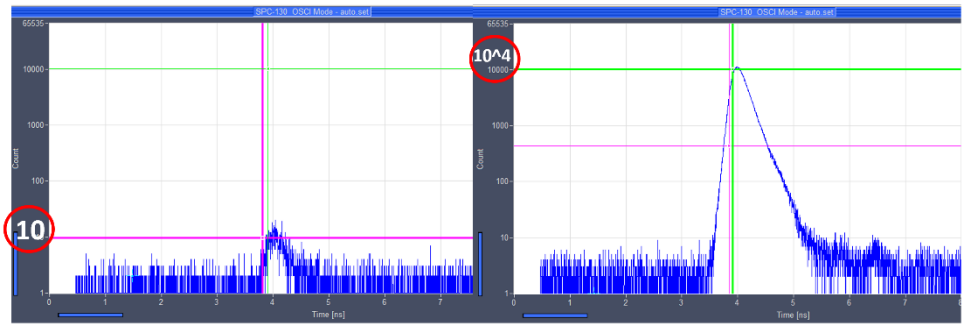

Fig. 37 amplitude signal difference between on (right side) and off state (left side) of DMD , both are plotted in logarithmic scale.

4 CHAPTER 4 – CHARACTERIZATION OF THE TIME DOMAIN RAMAN SPECTROMETER

Even if some hints on the system characterization have been already shown in the previous chapters, the complete characterization is presented here. It is divided into four sections, representing the four features that we considered to be most relevant in such a spectrometer. The first feature under analysis Is the Spectral Resolution, the second one is the Spectral Linearity of the device, relation between wavelengths and their positions on the DMD plane. The third feature is temporal resolution, it is very important to know the temporal behavior of the device since time domain techniques will be used. The fourth feature is a generic feature, reported in every optical device ad it is the Optical Efficiency.

The characterization reported here is related to Configuration_1. The same procedures have been applied to Configuration_2 but for the sake of clarity, only the final results will be presented for this configuration. Measures here shown have been taken with The Thorlabs fiber bundle 1.4mm x 200um and a 300 lines/mm transmission grating. To get images of the focused spots, the Newport laser beam profiler has been used.

4.1 SPECTRAL RESOLUTION

The system under analysis is a spectrometer, therefore one of the features of main importance is the wavelength resolution power (spectral resolution). In our case, given that the optical elements are perfectly aligned (DMD and Detector in the exact focal plane) the critical elements inside the device that will strongly conditionate the spectral resolution are: Grating, Fiber Bundle, and DMD's pixel pitch. The line density of the grating affects its dispersion power on light colors, the more the line density, the more light is dispersed on the focal plane, the easier it is to resolve nearby wavelengths. Fiber bundle dimensions, especially the lower one (diameter of the smaller

fibers) defines the minimum size of the spot generated by a single wavelength on the DMD, the smaller this spot, the easier is to discriminate it with a neighbor spot. Pixel dimensions of the DMD is not a limiting factor in our case. The DMD used here is an HD device 1920 * 1080 pixel resolution and the pixel pitch is 7.56 um. Given that the fiber bundle dimension is way above the pixel pitch, the fiber bundle lower dimension is the limiting factor. We will, therefore, call Fundamental resolution, the one given just by the DMD device and Absolute resolution, the one that results considering the fiber bundle ad the complete system. It is predictable that the fundamental resolution will be at least one order of magnitude stronger than the Absolute resolution.

In practice, considering that the spatial dispersion from 700 nm to 860 nm is 5.2 mm and that the pixels have a thickness of 7.56 µm, the Fundamental resolution, seen as nm per pixel (intended ad pixel column) can be retrieved from Eq.1

$$Pd \ : \ DispW \ = \ Fres \ : \ \Delta\lambda \qquad \textit{Eq. 11}$$

Where, " *Pd* " stands for pixel dimension, equal to the pixel pitch of the DMD, " *DispW* " is the dispersion width given by the grating, " *Fres* " is the fundamental resolution, our unknown variable and $\Delta\lambda$ is the wavelength range that falls into the Dispersion width taken into consideration. In Configuration_1, by inserting the following values taken from the characterization of the system:

Pd	*7.56*	*µm*
DispW	*5.20*	*mm*
Δλ	*160.00*	*nm*

Table 1

$$Fres \ = \ 0.23 \frac{nm}{pixel}$$

This represents the intrinsic system limitation due to the optical layout. In our case, using a fiber bundle with a lower dimension of 200 µm, the spot on the DMD for a given wavelength will have a lower dimension of 200 µm, approximately 26 pixels. This lead to the capability of resolving two different spots at a distance of 26 pixels that means **6,2nm** of Absolute resolution (*ABSres*). The Absolute resolution is given by the product between the resolving power of the system(dependent on the width of the fiber bundle) and the Fundamental resolution. In other words, the number of pixel columns occupied by a monochromatic focused beam on DMD times the fundamental resolution per pixel. The calculation can be seen in the following equation:

$$ABSres = Npix * Fres = \frac{Fd}{Pd}\left(\frac{Pd*\Delta\lambda}{DispW}\right) \quad Eq.\ 12$$

Npix = number of pixel columns occupied by a focused monochromatic beam.
Fd = fiber bundle lower dimension

By setting the following values :

Npix	*26*	*pixel*
Fd	*200*	*µm*

Table 2

We end up with a value of the Absolute resolution equal to :

$$ABSres = 6.15\,nm \quad Eq.\ 13$$

Given that the absolute resolution depends on many variables, the homemade spectrometer has got a lot of channels that can improve significantly its resolution. A great improvement would be to increase the line density of the grating, the dispersion power of the grating can be increased by three times if the density is increased up to 1200 lines/mm. Such a solution can be easily implemented. Given that with a 300 lines

grating only 30% of the DMD active area is exploited, by using a 1200lines grating the dispersion width will be approximately 15.6 mm for 160 nm range, that will fit perfectly in the 5mm * 16 mm DMD's rectangular active area. Another way of improving the absolute resolution of the system is by lowering the image spot on a monochromatic beam on the DMD (lowering Npix value). This can be done by using a fiber bundle with lower x - dimension. For example, using a 1.4 mm x 50 µm bundle, the resolution will increase by a factor of four, giving a minimum resolvable bandwidth of 1.6 nm.

In the optimal case with a 1200line density grating and 50um lower dimension of the fiber bundle it is possible to reach:

$$ABSres = 0.53\,nm \qquad \textit{Eq. 14}$$

4.1.1 The exact positioning of DMD on the focal plane

The position of the DMD on the focal plane of the first optical path of the system is of crucial importance, if the DMD plane is out of focus, it strongly compromises the spectral selectivity of the spectrometer. A procedure for verifying the position of the DMD plane directly with the hybrid detector was developed, it enables to characterize the system as a "black box", without using any external device.

The procedure consists in shining the DMD with monochromatic light (generated by the TiSa laser) and afterword, by scanning the area of the image spot on the DMD with subsequent micromirror slits it is possible to retrieve a curve of intensity of the signal versus the micromirror slit position. By exploiting this procedure it will also be possible to measure the spectral resolution of the DMD by noticing how many pixel slits are covered by the monochromatic light spot. The more pixels are covered (in terms of FWHM of the signal intensity) the less will be the system resolution. The DMD will be in the optimal position, on the focal plane when the minimum number of pixel slits are cover for a single monochromatic spot present on the DMD

plane. For the following measure, the scanning of the focused spot has been conducted with slits of twenty micromirrors columns with an integration time of one second. In *[Fig. 38]* it is possible to see the number of counts per second at each slit position. Different curves correspond to different

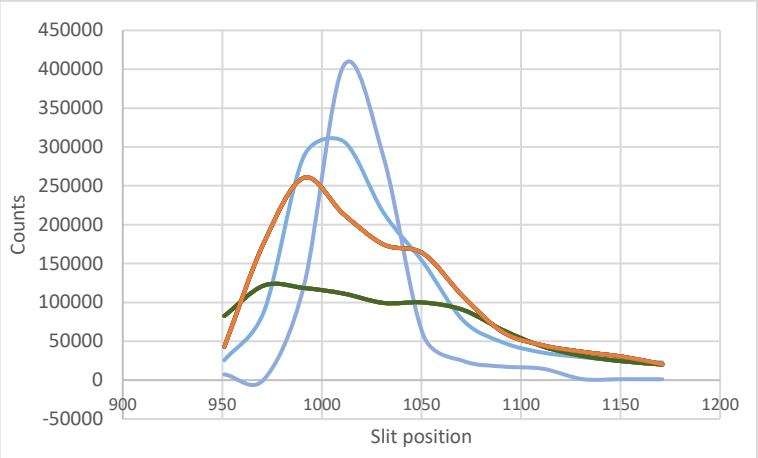

Fig. 38 light intensity of the focused spot over the pixel slit position. Different colours correspod to different DMD position along the optical axis, around the focal point.

the position of the DMD plane along the propagation axis and close by to the focal lens. The dark blue curve corresponds to the closest position to the focal plane, in fact, the focal spot is occupying the least number of pixel columns. Curves characterized by a larger FWHM show that the DMD plane is out of focus, therefore the focused spot is spatially broadened. It is important to point out that the distance on the propagation axis between the DMD positions in case of the orange curve (100 pixels FWHM) and the dark blue curve (26 pixels FWHM) is just about 1mm. This shows that the dimension of the image spot is very sensitive to DMD position. Remember that each pixel has a dimension of 7.56 um, therefore, the spot dimension at the best DMD position comes out to be approximately 220 um that is in great accordance with the 1:1 imaging system of the fiber bundle in use.

4.2 SPECTRAL LINEARITY

In order to have a detailed characterization of the system, a study on the focal spot on the DMD for different wavelength have been carried out. In particular, high importance has been given to the characterization of the x-axis dimension of the spot (parallel to the dispersion axis) at different wavelengths and to the centroid position of the spots for all the spectral bandwidth given by the TiSa laser. *[Fig. 40]* gives a better understanding of the variables taken into consideration; different images of the fiber tip at different wavelengths are dispersed on the image plane. Y-dimension corresponds to the bigger dimension of the fiber bundle, and x-dimension is related to the smaller one colors disperse on x-axes. The variables of the following graphs, used for the spot characterization are described. The x-dimension represents the diameter dimension of the small fibers, y-dimension the higher dimension of the fiber bundle and the dispersion axis lies on the dispersion plane of the grating, perpendicular to the direction of propagation of the beam.

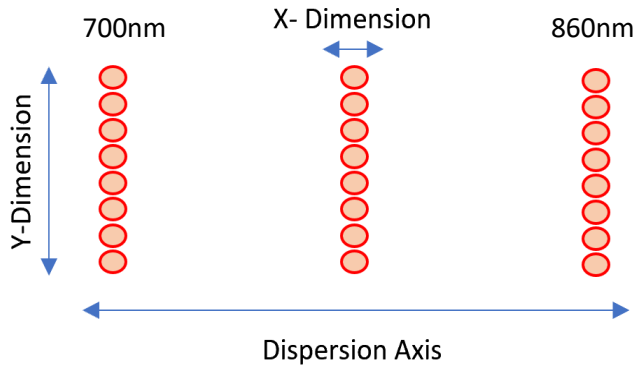

Fig. 39 Scketch of the dispersion of light on the image plane on DMD surface.

In *[Fig. 41]*, the centroid positions on x and y-axis have been measured at different wavelengths, scanning from 700 nm to 860 nm with steps of 20 nm. Wavelength tunability was possible thanks to the features TiSa tunable laser. From the picture, it is possible to see that the centroid positions on the y-axis do not undertake significant changes related to wavelength tuning. This is expected, given that the dispersion direction of the grating

lies on the x-axis, no translation on y-axis means that the grating is well aligned. The centroids x-dispersion have a linear behavior related to the tuning of the wavelength.

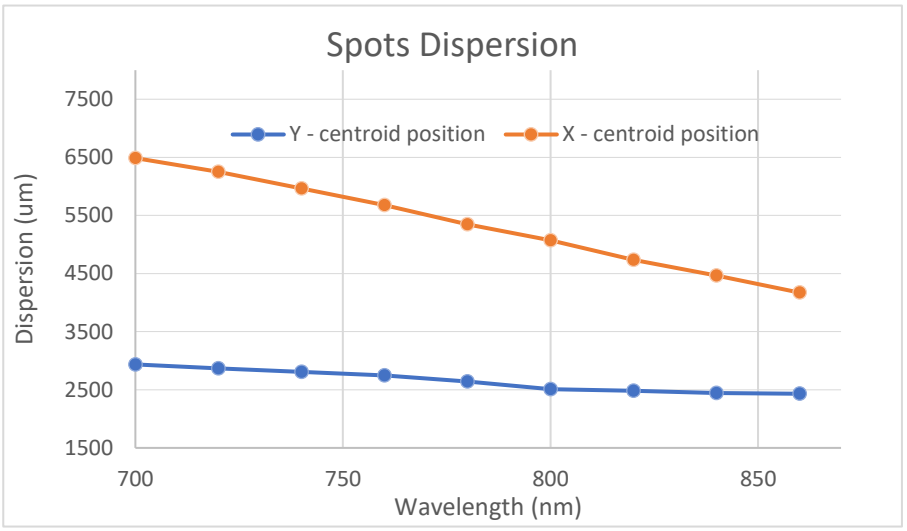

Fig. 40 Centroid position on DMD plane on x and y axis versus wavelength

This behavior will be extremely important when it comes to the spectral selection of the incoming diffracted beam. In fact, thanks to the linearity, once the system is calibrated, it will be straightforward to predict the position of a particular wavelength on the DMD plane. The exact characterization of the wavelength position, related to micromirror columns on the DMD is shown in *[Fig. 42]* where the data collected show a strong linearity between wavelength and pixel position (on x dimension) on the DMD. On the graph is shown the linear regression line related to the data points and the equation of the regression line is shown on the top right corner. As it can be noticed the Coefficient of Determination R squared has very high value, this suggests that regression predictions approximate very well the real data points. Therefore, linearity between the two variables is a valid approximation.

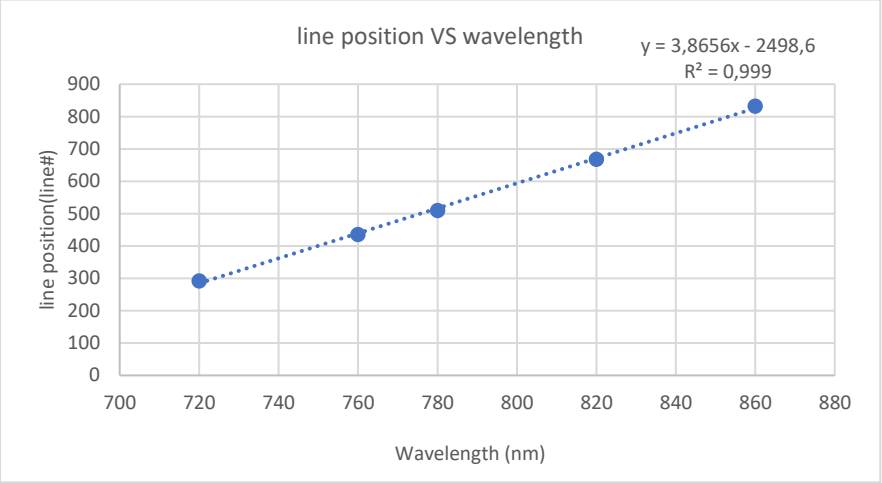

Fig. 41 line position of the centroids of the laser spot at different wavelengths. Equation of the regression line on the top ight corner.

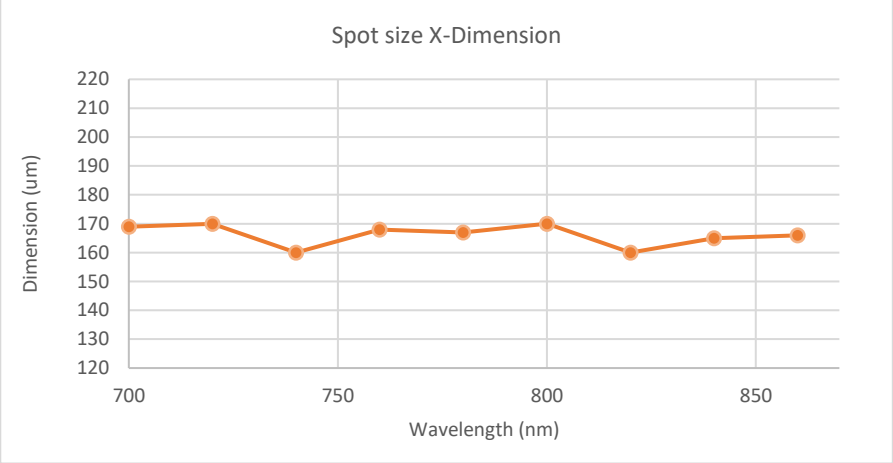

Fig. 42 FWHM on the x-dimension of the spots on the image plane.

In *[Fig. 43]* are shown the different values as FWHM of the spot size on the DMD plane x-dimension. It is good to see that the values do not change significantly at different wavelengths and that are all under 200um (lower dimension of the fiber bundle tip), it suggests good alignment of the system.

4.2.1 Focusing system on hybrid TCSPC Detector

The characterization of the second branch of the spectrometer, including the focusing of the beam reflected from the DMD on the hybrid TCSPC Detector's active area, has also been done by acquiring images of the

focalized spot at a different wavelength on the focal plane. Even though very important for the correct functioning of the device, the alignment of the second branch is less critical than the first one. Given that the detector used is a single pixel device, the shape of the image impinging on the pixel does not matter, in terms of information that can be retrieved. the most remarkable feature is that the focused spot of all the wavelength range must fall into the detector active area. If not, we will unavoidably incur in loss of signal intensity, therefore loss of information.

From the characterization, it has been possible to verify that also on the detector plane that spot position on the x-axis versus tuned wavelength presents a linear behavior and the dispersion width is reduced a lot due to the different optical system. In fact, the dispersion width for a given wavelength range of 160 µm is 1.2 mm, nearly a fifth of the dispersion width on the DMD plane. The system has been designed to be able to detect a broad wavelength range with the small active area (3 mm diameter) of the detector as described in *chapter 3*.

In *[Fig. 44]* are shown the spots of tow monochromatic beams and the edges of the wavelength window. In the white boxes are shown the position of their centroids. The y-axis is the axis parallel to the dispersion axes (inverted from before). By subtracting the two y values of the centroid positions at 700 nm and 860 nm it is possible to retrieve the dispersion width for a $\Delta\lambda$ of 160 nm.

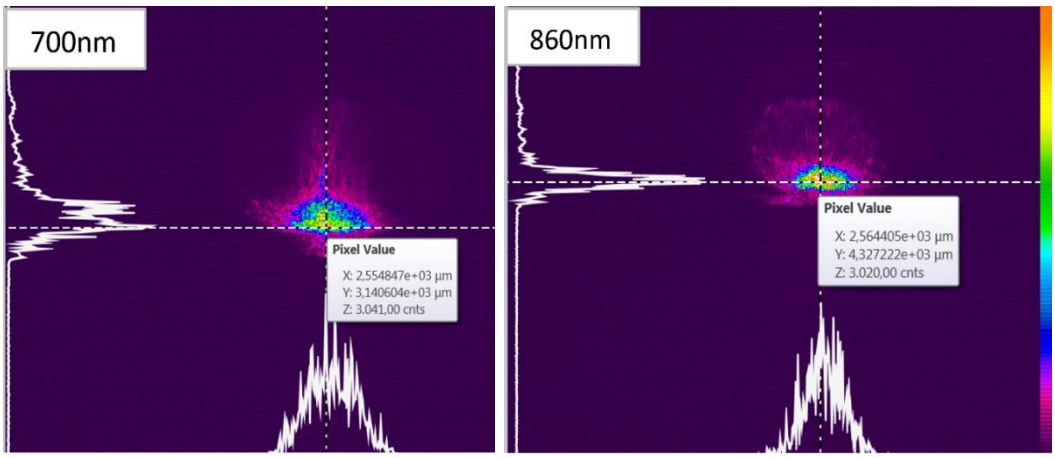

Fig. 43 Laser beam profile of the image spot on the detector active area, at two different wavelnenghts 700 nm and 860 nm

It has been seen that even though aberrations are present, the FWHM on the y dimension of the spot in lower than 70 μm for all wavelengths this is a good result and with a total dispersion of 1.2 mm it will be sure that no losses of information will occur.

4.3 TEMPORAL RESOLUTION

Having insights on the temporal resolution of the device is of main importance since it will define the working features and limits for time domain measures. To be able to state the temporal resolution of the spectrometer, it has been acquired the impulse response function, TCSPC curve, of the whole system. The Fiber bundle has been coupled directly to the outcoming laser beam. The laser has been set to Mode-Locked mode and aligned to have pulses as short in time and stable as possible. Considering that the time pulse width if the Mode-Locked mode can reach 60 ps, the resolution of the whole system will be only limited by the IRF proper of the detector and eventually by pulse broadening due to the optical path inside the spectrometer.

4.3.1 IRF of the spectrometer

The IRF of the whole system is shown in *[Fig. 45]* and it presents an FWHM of 199ps that as expected comes out to be broader in time that the IRF of the detector itself. As it can be appreciated the dynamic range is approximately 3 decades and in the free running acquisition (counts axis in log scale) there are no intense reflections that could interfere in the measures.

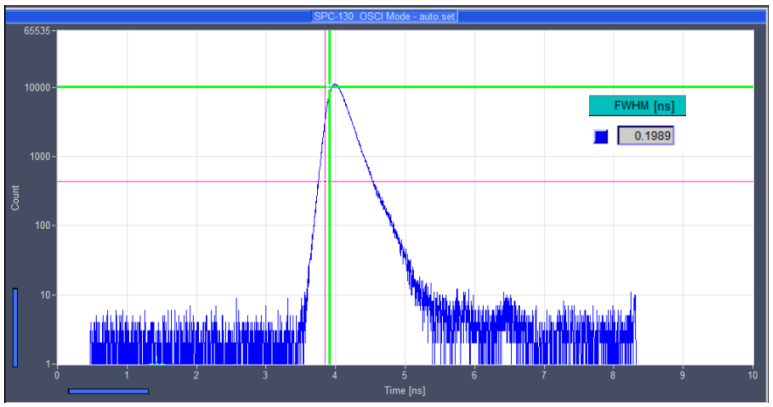

Fig. 44 IRF of the homemade Raman TD Spectromter

4.3.1 System operation Times

Considering the possibility of the DMD to work at a rate of 9500 Hz with preloaded patterns and that our working time for integration of the signal will at the minimum, fractions of a second. There will be a difference of approximately four decades between our minimum working time and the dead time of the DMD. Therefore, considering that in our measures we will always use the preloaded pattern mode (patterns are charged in the memory of the driver before being shown on the DMD) we can say that dead times in pattern display are negligible for our purposes.

4.4 Optical Efficiency

Optical efficiency is a crucial issue when dealing with diffusive Raman, however, signal intensity in our TD Raman spectrometer is very strong. This is not common and it is probably due to the powerful spectrometer and high Raman signal probes that we are using in our setup.

4.4.1 Optical efficiency comparison between the two Configurations

Configuration_1 starts as a 2/f system coming out of the fiber bundle and collimated with a D50 F100 lens. After collimation, an optical Iris is set before the grating, in order to diminish the diameter of the beam to D25 (dimension of the grating). because of this intervention, the system is transformed into a 4/f optical setup. The effective efficiency of configuration_1 (*Eff_C_1*) came out to be:

$$Eff_{C_1} = \ 2.37\%$$

From *[Table 3]* it is possible to see the contribution of dumping efficiency of the different optical elements. The aperture limiting the beam dimension is the less efficient in the system, it is the reason why in the second configuration the layout has been changed in order to make the system f/2.

Element	Efficiency	
Aperture	0,18	Measured
Grating	0,65	From Datasheet
DMD	0,46	Measured
focusing system	0,54	Measured
Fiber + optics	0,8	Estimated
Aperture + DMD + Grating	0,054827	Measured
Total	0,024	Measured

Table 3 Efficiency of configuration_1

The efficiency in Configuration_2 (*Eff_C_2*) has been increased significantly, it has nearly doubled thanks to the removal of the aperture, reaching a value of:

$$Eff_{C_2} = \ 4\%$$

5 CHAPTER 5 – RAMAN SPECTRA AND OPTIMIZATION

Once the device was built, and the full characterization was completed measures of samples begun. As the first step, we decided to acquire Raman spectra with the device exploited as a monochromator spectrometer, the samples under analysis have been chosen from materials with high Raman cross-section, materials such as Titanium dioxide and Marble. Measures have been firstly conducted with the use of a microprobe (see *Appendix*) as a Raman signal collector. Once the first satisfying Raman spectra where acquired, as the second step, diffuse Raman spectra, acquired with microprobe (see *Appendix*) have been acquired, eventually analyzing bilayer scattering samples.

The last step consisted of the implementation of the compressive sensing software and algorithm into the spectrometer. Due to lack of time, only some spectra have been acquired but the results are noteworthy.

Measures have been carried out with the system in its second configuration (Configuration_2) because it has been chosen as the most performing layout.

5.1 RAMAN SPECTRA WITH MICROPROBE

The spectrum of Raman emission of Titanium has been recorded. Raman signal has been stimulated with a 100Mhz pulsed beam tuned at 785 nm and it has been collected throughout a microprobe. The expected Raman spectra present four peaks in the same position as the ones shown in *[Fig. 46]* The peaks will be surely less resolved and the raw spectra can be covered by fluorescence or straight light present inside the spectrometer.

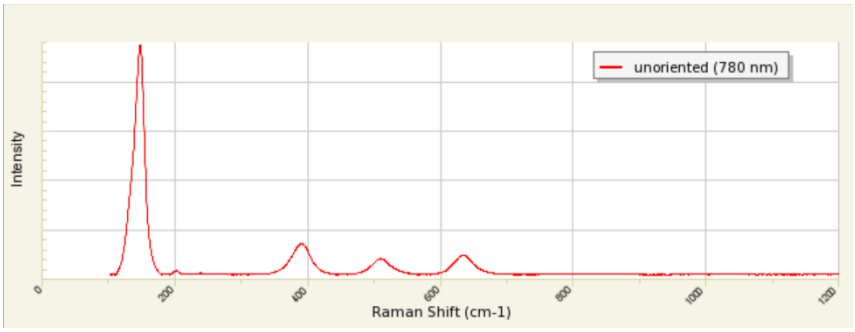

Fig. 45 Raman spectra of TiO_2 unoriented with excitation beam 780 nm, the following graph has been taken from: http://rruff.info/anatase/display=default/R120013

In our measure, the peak of the excitation beam at 785nm has been characterized with the spectrometer. The spectral profile can be seen in *[Fig. 47]* (blue curve). The DMD has been utilized rotated by 45 degrees on it's normal to have the on-state on the same plane of the incident beam (Configuration_2). The single pixel line dimension will then be bigger than the dimension of the pixel. Approximately 10 µm. (instead of 7.5 µm) but it does not influence in any way the Absolute resolution of the system.

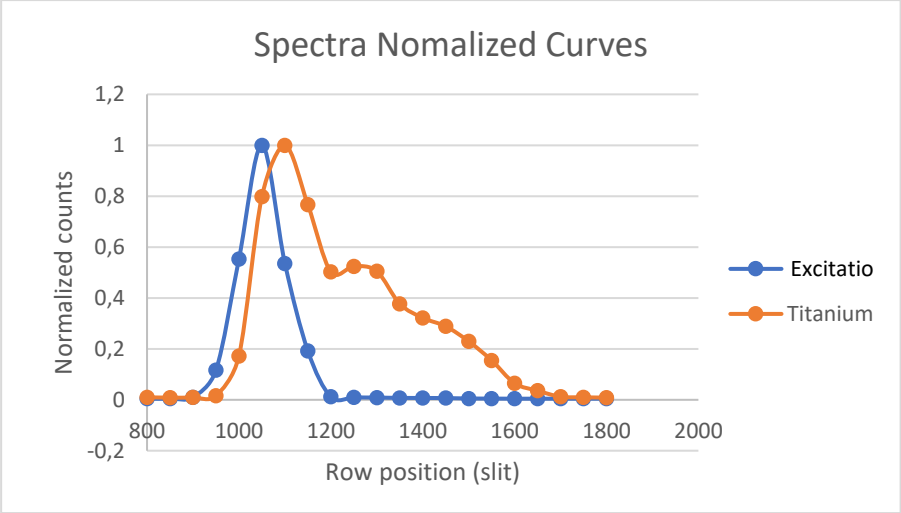

Fig. 46 Normalized spectral curves of Excitation beam and Titanium Raman spectra.

To retrieve the spectrum of the sample and of the excitation beam the spectrometer has been used in monochromator mode. The DMD has been divided in slits (50-pixel lines, duty cycle 5%, higher than the maximum resolution for a faster measure) and the slits have been opened sequentially

from one extreme to the other of the spectral image. Scanning all the spectrum with one second integration time per slit, the curve in *[Fig. 47]* have been retrieved, total measurement time of thirty-five seconds.

Titanium has a strong Raman peak very close to the wavelength of the excitation peak 785 nm, so close that in this configuration we couldn't discern the two peaks, that coincide in raw position 1150. It is evident the presence of Raman Photons in the region of the spectrum away from the peak (position range 1300 to 1600) wavelength and the intensity of the Raman photons is also significant. The curves plotted on the graph have been normalized to simplify the understanding of the phenomena, with the original photon counts the peak of the excitation beam would have been three orders of magnitude more intense than the Raman peaks.

The main problem of the system is that even when the DMD is in off state, some stray light is still present on the background that covers Raman signal. By further improving the optical setup it was possible to enhance Raman signal to noise ratio. The DMD position has been accurately optimized in order to put it exactly in the focus position. In this way, the spectral resolution has been enhanced reaching a spot size on the DMD of approximately 210 µm. It was possible to evaluate the spot size, by sequentially opening small slits of the DMD and read the number of counts on the detector as explained in section *4.1.1*.

An important addition has been done to the photon collecting system (microprobe). A color filter high pass filter with a threshold at 830nm has been inserted into the microprobe focusing system. The addition of this element made it possible to see also the peaks with significantly lower intensity and with higher Raman shift. It was also possible to reveal the peak nearby the excitation wavelength. The results can be seen in *[Fig. 48]*

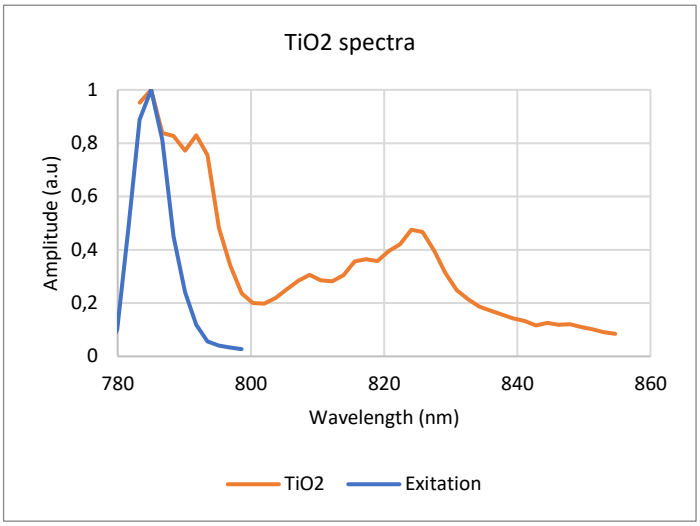

Fig. 47 Spectras of exitation beam and TiO2 spectra, with the implementation of the color filter.

It is also interesting to see an increasing intensity behavior at a wavelength greater than 800 nm. This phenomenon can be explained by taking in to account the filtering spectral profile of the interference filter. In fact, the filter in our disposal has got a dump in filtering efficiency exactly in the wavelength range between 800 and 830 nm.

5.1.1 Effect of the Spatial Filter on Detector Active Area

Straylight issue persists, despite the optimization applied so far. Hence, it has been decided to implement a further modification: spatial filtering of the excitation beam directly on the detector active area in order to avoid excitation stray light impinging on the detector. The focusing spot on the detector position of the exiting wavelength has been studied with the beam profiler Newport camera and it has been seen that it is sufficiently confined to be filtered out. The modification has been applied to the system in Configuration_2, the dispersion direction is set therefore on the vertical axis (because the grating has been rotated by 90 degrees) In the *[Fig. 49]* a sketch of the spatial filtering applied on the detector active area is shown in order to make it easier to be understood.

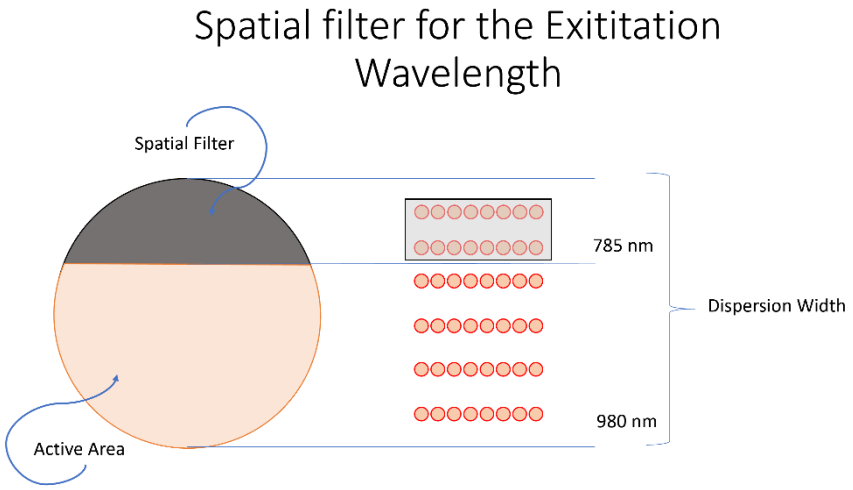

Fig. 48 Sketch of the spatial filtering implementation on the detector active area. The black spatial filter on the top of the detector active area is filtering out the unwanted wavelengths

As it can be seen, the spatial filter has been ubicated on the top of the active area where excitation wavelength is dispersed. By moving the detector on the vertical axis, the threshold of the filtered out wavelength rage can be tuned.

A new measure has been carried out on the TiO_2 sample, using the Microprobe. For this measure, 10-pixel width slits (duty cycle 3%) have been used, with one second integration time per slit. With 10-pixel slits width, a higher resolution scan has been conducted compared to the absolute resolution: 26-pixel rows. Resulting measures from the implementation of the spatial filtering are analyzed in the following paragraphs. A great improvement of resolution can clearly be seen in *[Fig. 50]* due to better alignment of DMD on focus and detector on the focus plane. Plus it is possible to see the effect of the spatial filtering on the detector. By moving the spatial filter it is now possible to clearly select the region of excitation wavelength and filter it out.

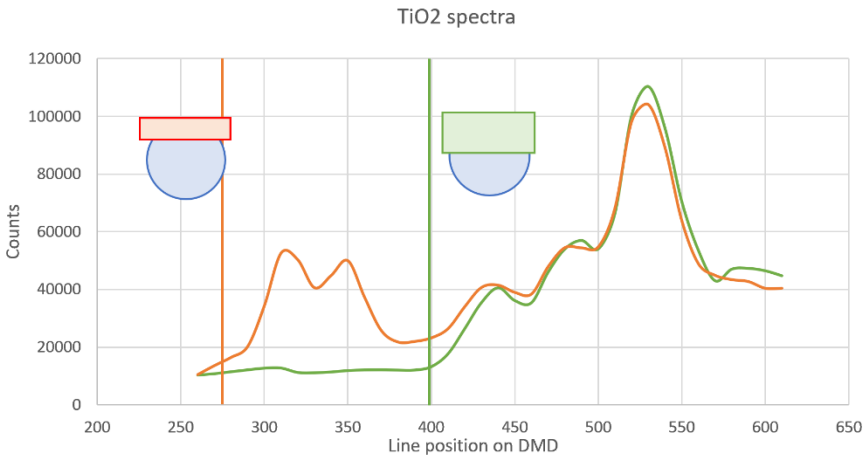

Fig. 49 Raman spectras of TiO_2 are shown related to two different position of the spatial filter. The straight vertical line show the projection of the spatial filter edge on the DMD plane. On the side of the straight line, a sketch of the spatial filter position on the detector active area is shown.

From the measures, it is possible to conclude that the spatial filter implementation gives a strong help in accurately removing stray light coming from the excitation beam. It helps in giving a better contrast to the Raman peaks with lower intensity, eventually achieving a better visualization of the spectrum. The two peaks at 310 and 350 line position sown on the orange curve are related respectively to part of the stray light coming from the excitation beam (line 310) and the first Raman peak of TiO_2 that was not present in *[Fig. 47]* and was not efficiently discerned in *[Fig. 48]*.

5.2 RAMAN SPECTRA WITH MACROPROBE

Raman signal collected from microprobe is known to be a strong signal. In case of non-scattering media (TiO2 is an example), the excitation beam is spatially confined on the surface of the media and because low number of scattering events happen and, Raman photons, only travel very short distances into the material and from superficial generation regions, go directly into the detection fiber through a short path in air. In diffusive media, the excitation beam enters the media and, scattered in all direction the photons travel through the phantom. Depending on the detection

position of the collecting fiber, only photons characterized by certain high probability paths are detected after they have been absorbed by molecules and reemitted as Raman photons trough out their whole path. The most probable path between to points is the so-called banana shape path *[Fig. 3]*. Raman photons are therefore generated through all the path in different places, not only around the focus of the excitation light.

In diffuse media, when the distance between injection and collection (ρ) is not zero (ρ ≠ 0), the excitation beam, due to scattering can show a significant dump in amplitude compared to the intensity seen in microprobe (ρ = 0). For the probe used in the experiments, designed and built in our labs (see appendix - macroprobe), the focus plane is set approximately 15 cm apart from the lens system. The excitation beam intensity profile is shaped with an axicon lens to image a ring of variable radius. The radius of the ring can vary by moving the collimation setup including the axicon lens along the rails, enabling SORS measurements. In our measures, we will set the ring to have 5 mm in diameter and approximately 1 mm in thickness. The collection region is the center of the ring. Thanks to the particular shape, we will be able to collect diffused Raman photons from the enlighten ring to its center, hence it will be possible to probe a deeper layer of the phantoms.

Following the example of a Raman study conducted by Politecnico Di Milano Laboratories [5], It has been chosen to use some already made phantoms. Marble: *Calcite, $Ca(CO_3)$* [μa = 0.04 cm-1 and μs' = 12cm-1] and poly dimethyl siloxane (PDMS) [μa = 0.05 cm-1 and μs' = 8 cm-1] have been chosen as first materials to be analyzed by the homemade TD Raman spectrometer. Silicone elastomer has been used commonly in diffuse optics and Raman spectroscopy to mimic tissue optical properties [52]. The scattering properties of PDMS were tailored to be μ'_s = 10 cm−1 (typical near-infrared scattering of biological tissue) at 700 nm, which was achieved by mixing a mild quantity of TiO2 powder to the PDMS recipe.

5.2.1 Marble and PDMS

The relative spectra of the two phantoms retrieved by the homemade Raman spectrometer are shown in *[Fig. 51a]* for the Marble and *[Fig. 51b]*for the PDMS phantom. Measures have been taken with 40 seconds integration time per slit for Marble and 60 seconds time integration for PDMS the difference in integration time can explain the higher number of counts in the PDMS spectra. As it is possible to see in the pictures Marble spectra is characterized by an intense peak at 1040 cm-1 shift position from the excitation beam that corresponds to line 710 on the DMD. For silica instead, the Raman spectra are characterized by two less intense peaks that lay on slit position 775 and 830. For easier comparisons between different data, the x-axis of the spectra will always be presented as a slit position and not inverse wave number. The conversion can be executed with the data acquired in the DMD characterization section ***Errore. L'origine riferimento non è stata trovata.***.

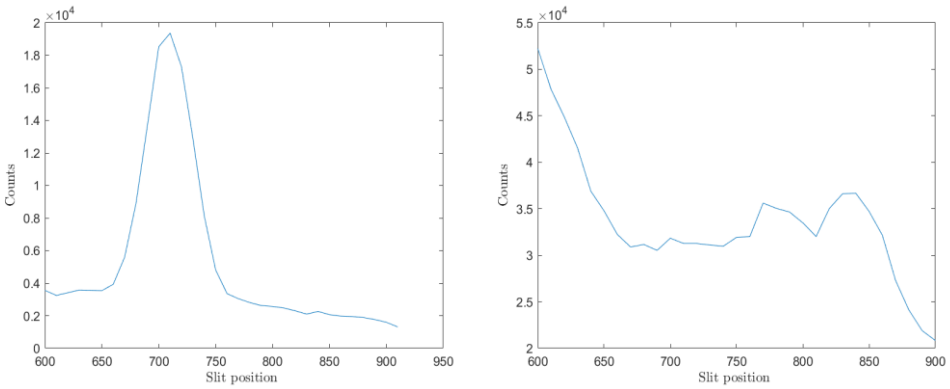

Fig. 50 a) on the left Marble raman spectra. b) on the right PDMS Raman spectra

Spectra above have been taken with a duty cycle of 3.3%, spectral resolution and sensitivity of the detector are enough to retrieve the Raman spectra needed for our purposes. It is important to notice that the peaks of the two spectra are all at different slit position. This complementarity of the spectra will be useful in future. Next step, in fact, will be the spectral analysis of the bilayer phantom, made by the union of the two above studied materials. Complementarity of the spectra is needed in order to be able to distinguish the contribution of different material to the spectral image.

5.2.2 Multilayer

Given that with our system and the explained procedures it is possible to see clear Raman spectra in the wavelength region of our interest, and driven by the interest in probing deep layers in the diffusive matter; it has been decided to conduct measures on a bilayer phantom made up by the previously studied materials. The phantom is composed of an upper layer of PDMS 5 mm thick and a bottom layer of calcite, Marble CaCO3.

Properties of the Top layer and lower layer: PDMS		
μ_a	0.05	cm-1
μ_s'	8.0	cm-1

Table 4

Properties of the bottom layer and lower layer: Marble		
μ_a	0.04	cm-1
μ_s'	12.0	cm-1

Table 5

The measured time has been increased by nearly double with respect to the previous measures. The system has been set so that the subsequent patterns will create a monochromator like working regime. The slits are made of 10 pixels (3.3% duty cycle) and each slit will stay on the on-state for 80 seconds, giving a total integration time of approximately 40 minutes. Integration time has been increased to improve the signal to noise ratio, expecting a worse SNR for the PMDS peaks due to Marble peak stray light. The number of counts per seconds was 4000cps for Marble (bottom layer) and 2500cps for the upper layer of PDMS.

The raw spectrum retrieved from the measurements is shown in *[Fig. 52a]* and in *[Fig. 52b]* the same spectra is plotted with background correction for a better visualization.

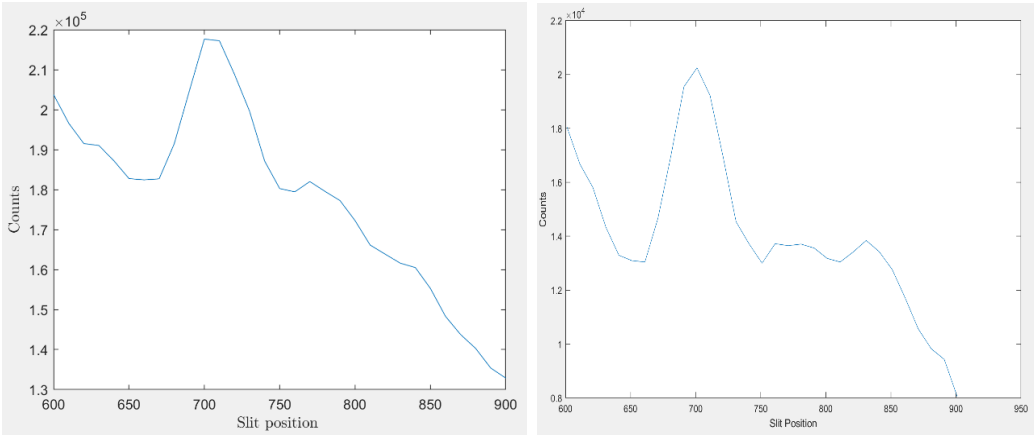

Fig. 51 a) on the left, the raw bilayer phantom Raman spectra. b) corrected bilayer phantom Raman spectra, for better visualization.

From the above pictures, we can clearly see the contribution of both the layers. The marble peak (bottom layer) has got very high intensity, and the PDMS peaks can clearly be distinguished.

Exploiting the time domain features of our device, a time gate of the region of interest of the TCSPC diffusion curve has been applied to the measurements with the aim of separating the two spectra by analyzing first the early photons (scattering into PMDS) and secondly the late photons (coming from the Marble bottom layer). In particular, it has been chosen a time gate of 100ps. Results can be seen in *[Fig. 53]* where it is possible to appreciate a stack of the Raman spectra related to different time gates in *[Fig. 53]* Early gates are shown at the bottom of the picture and they carry information on the upper layer. Whereas on the upper side of the picture we can appreciate late gates, corresponding to bottom layer information.

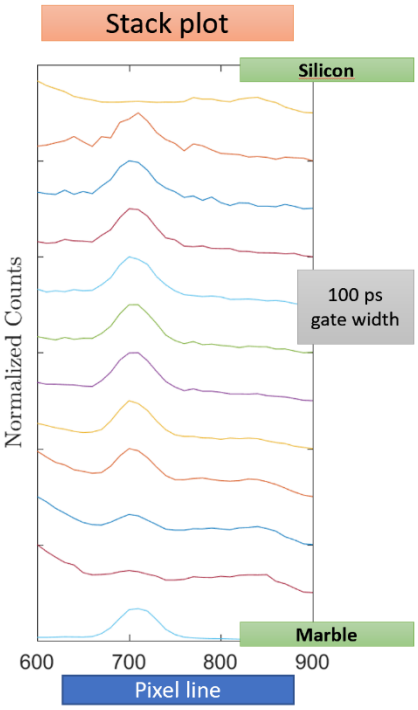

Fig. 52 Normalized stak plot of the spectra at different time gates.

Another effective way to better visualize the contrast of Raman signal either of the Marble or Silicon peaks is shown in *[Fig. 54]* In where all the curves at different gates are plotted without any normalization.

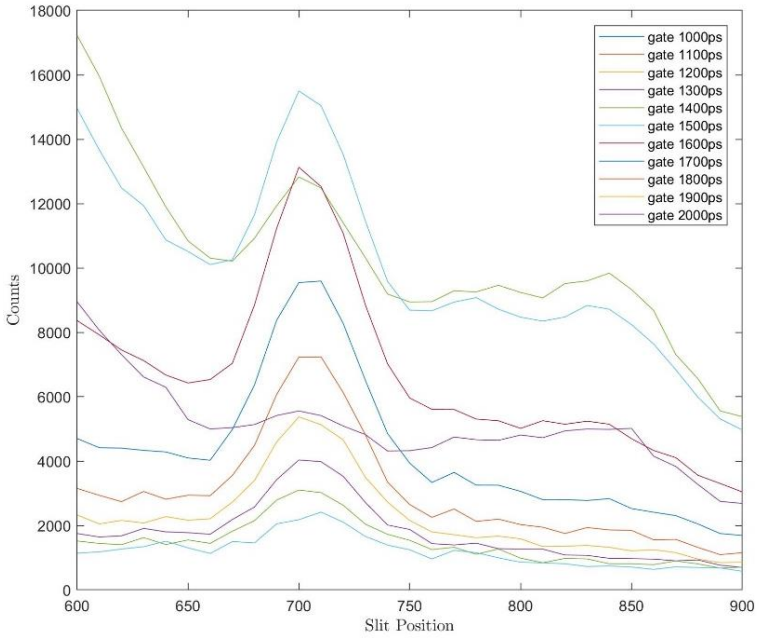

Spectral curves of different gates are plotted in different colors, information can be retrieved from the legend of the picture. As it is possible to notice, I the first 3 gates, silicon packs have a very high contrast and can clearly be distinguished. Marble peak from gate 2 starts increasing rapidly till it is the only one visible at gate 4 reaching its maximum contrast at gate 5. For later gates, the intensity of the marble peak decreases till gate 10.

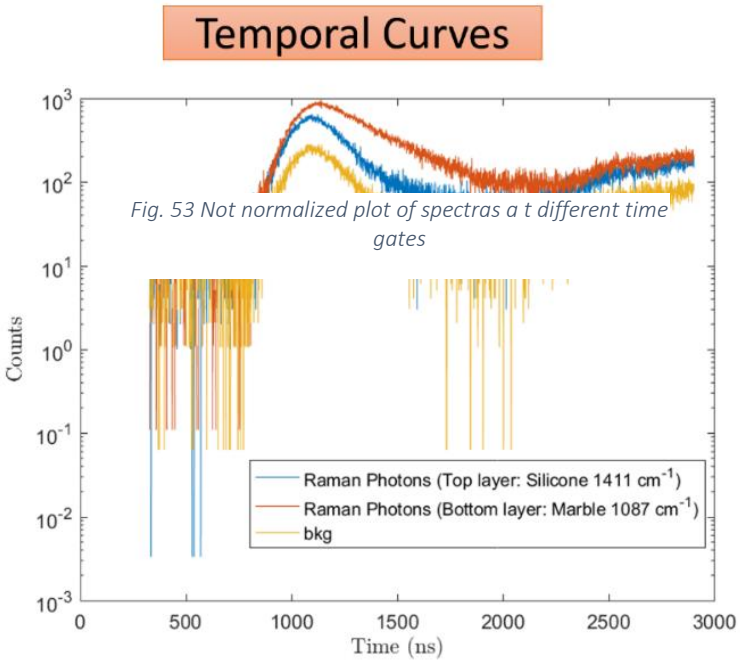

Fig. 53 Not normalized plot of spectras a t different time gates

Fig. 54 TOF curves at different wavelength posiions wher a dominant contribution of Marble, Silicon and nois is present respectivelly

[Fig. 55] shows the temporal curves (TOF), retrieved by selecting a certain wavelength range (or slit position) to get the contribution of marble, silicon, and background respectively. As it is possible to notice, we clearly see an important diffusion tail in the marble region of the spectra, while it is a lot less noticeable in the silicon peak, and even lesser, as expected, where the background contribution is dominant. Notice that due to DMD features even in the background we will have stray light from Raman signal that will modify the background counts. This stray light is also the main reason for the low dynamic range that we can appreciate in *[Fig. 55]*. Notice that the strange behavior at the end of the curve, raising ramp, must be due to sinc

oscillations, that can go out of alignment probably due to the slight instability of laser mode during the measure. When out of alignment, the sinc could also create artifact like reflections or raising intensity ramps in the TCSPC curve due to electronic noise.

A measure of the bilayer phantom has been done also with the microprobe in order to see whether the difference between the two signals intensity is significant. The contrast between the layers can (early and late gates), in this case, be better highlighted. The results can be seen in the following figure *[Fig. 56]* where it is possible to appreciate the two cases of gated curves.

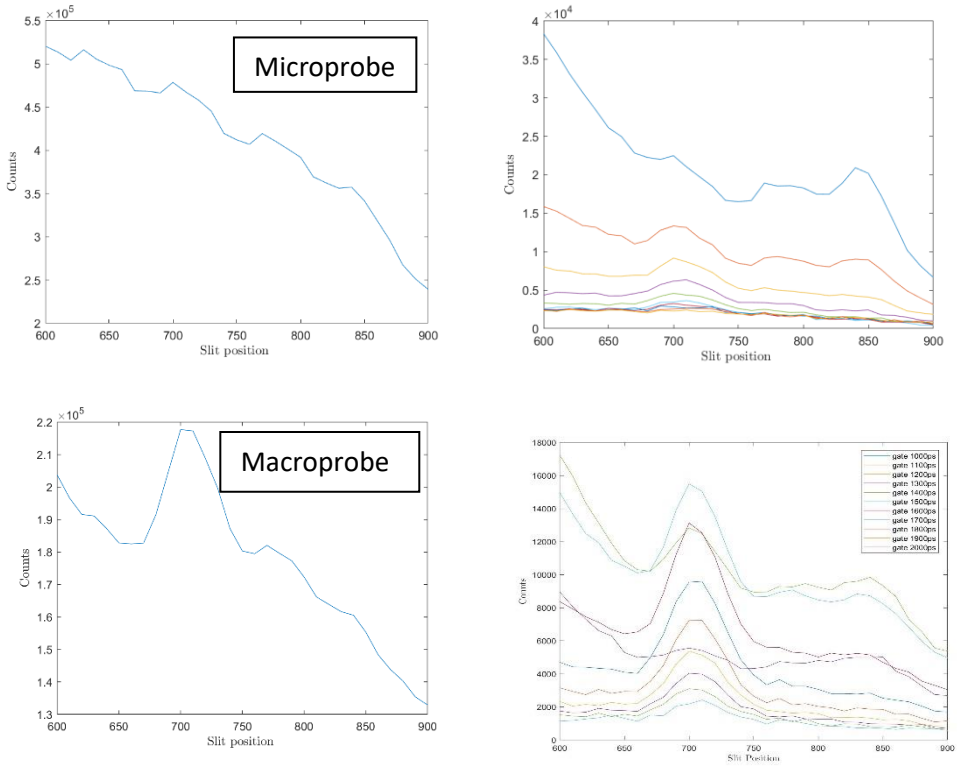

Fig. 55 Comparison between Raman Spectra collected with Microprobe, first row, and Macroprobe, second row. Raw spectra are reported in the first column and time gated spectra in the second column.

In the microprobe, that is more sensitive to the surface layer, we can see a relatively lower contribution of the deep player of marble, compared with the upper layer of silica, as expected. The peaks of PMDS collected with the microprobe result very evident in the first gates and remain present for the

first four gates. Marble peak comes out already in the second gate, but its contrast results a lot lower than in the case of the macroprobe.

It is interesting to see how the behavior of the curves related to different gates differs between microprobe and macroprobe. In the macroprobe, the intensity of the Marble peak is so high that more Raman photons are retrieved in late gates compared to early gates. In *[Fig. 56]* the graph on the bottom right shows that for early gates, we see PMDS peaks with low average counts, and counts increase with later gates. Since maximum average counts are achieved at gate 3. After the third gate, the average number of counts decreases until the noise covers signal. In the microprobe instead, the peaks of PMDS and Marble are of comparable intensity, the graph on the top left. This translate in higher average counts for early gates (typical in microprobe configuration) and a progressive lowering of the average counts for later gates.

5.3 COMPRESSIVE SENSING MEASURES

In the last part of the project, it has been decided to update the software for the DMD control to be able to upload the pattern for compressive sensing measurements. Hadamard patterns will be used (see section *1.6*) and the system will face a significant increase of duty cycle, from 3% to 50%. Thanks to a higher duty cycle, compressive sensing will enable faster measurements. In this chapter Compressive sensing, Raman spectra acquisitions in the time domain are shown. A set made up of the first 32 two dimensional Hadamard pattern has been used and the reconstruction of the spectra have been possible thanks to a self-developed MATLAB code, exploiting inverse Hadamard transforms.

5.3.1 C.S. Raman Spectra

The measure has been conducted with the same hardware set up and phantoms used in section *5.2.2*. The Macroprobe have been used and the bilayer phantom have been taken in to study:

Properties of the Top layer and lower layer: PDMS		
μ_a	0.05	cm-1
μ_s'	8.0	cm-1

Table 6

Properties of the bottom layer and lower layer: Marble		
μ_a	0.04	cm-1
μ_s'	12.0	cm-1

Table 7

Hadamard 2D patterns have been created with MATLAB as 2D matrixes in logical units, to be plotted on the DMD. A negative 2D matrix (reversed intensity of the pixels 1 -> 0 and 0 -> 1) has been created for each Hadamard pattern. To be able to make the full reconstruction of the spectra, both the positive pattern and its negative version have to be plotted on the DMD.

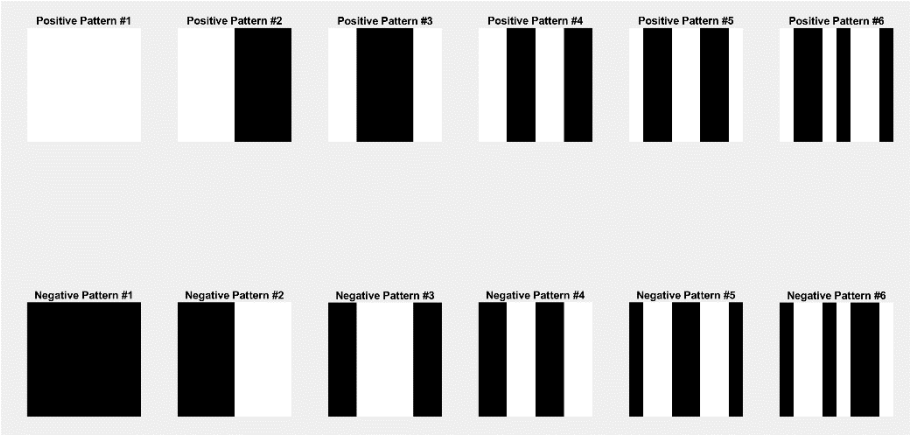

Fig. 56 2D Hadamard patter, matrixes to be plotted on the DMD. White color rapresent logical value 1, that correspond to on mirros state of the DMD. Black pixels represent DMD off-state.

For each pattern, it will be possible to acquire a time of flight curve of the incoming photons intensity. From the integral of the TOF curve, it will be possible to give a weight (multiplication coefficient) to each pattern, that will be used for the reconstruction of the spectra with the Hadamard

transform. The weight of each one of the 32 patterns is given by a simple linear combination between the integrals of the curves of the positive pattern and its negative version.

In order to have good signal intensity, five seconds integration time for each pattern has been chosen making the total measuring time four times shorter compared with the measures taken in monochromator mode, from 40 minutes to 10minutes. Between each pattern, a tag pattern of three seconds has been inserted to be able to distinguish the counts measured in time.

It is possible to see the reconstructed spectra retrieved from a 10 minutes measurement in the following picture.

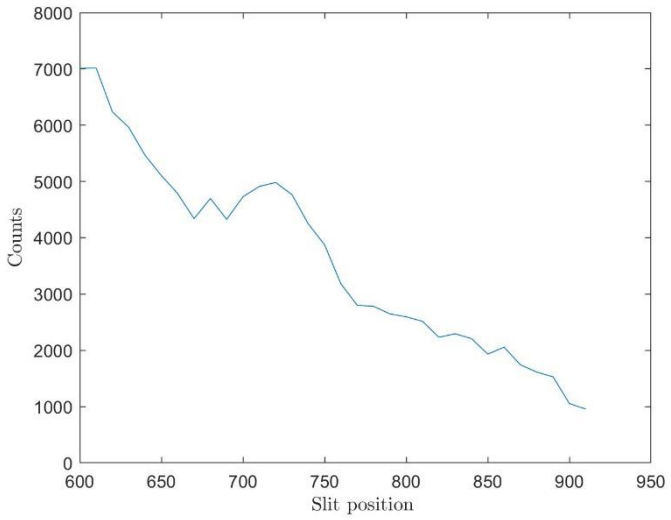

Fig. 57 Spectra retrieved from Compressive Sensing measure.

As expected, the noise in the spectral intensity distribution is greater than in the monochromator mode acquisition, this explains the spikes before the marble peak and in between the two PMDS peaks. Overall the construction is satisfying, the peaks can be distinguished even though the signal to noise ratio is worse. A possible improvement, to have a better SNR on the spectral curve, can be made by assigning the same integration time for each pattern that was used for the monochromator mode.

5.3.2 T.D. C.S. Raman Spectra

For the Compressive sensing measures, the time domain analysis of the collected data has been conducted in a similar way as the monochromator like measures. The background has been subtracted from all the curves and a region of interest (ROI) have been selected around the peak of the TOF curve. (+- 500 ps). The curves have then been divided in time gates of 100 ps before the Hadamard reconstruction have been realized. Once retrieved ten temporal gates for each pattern, the Hadamard transform has been applied and the one reconstructed spectra for each gate have been retrieved. In *[Fig. 59]* the reconstructed spectra at different time gate can be appreciated.

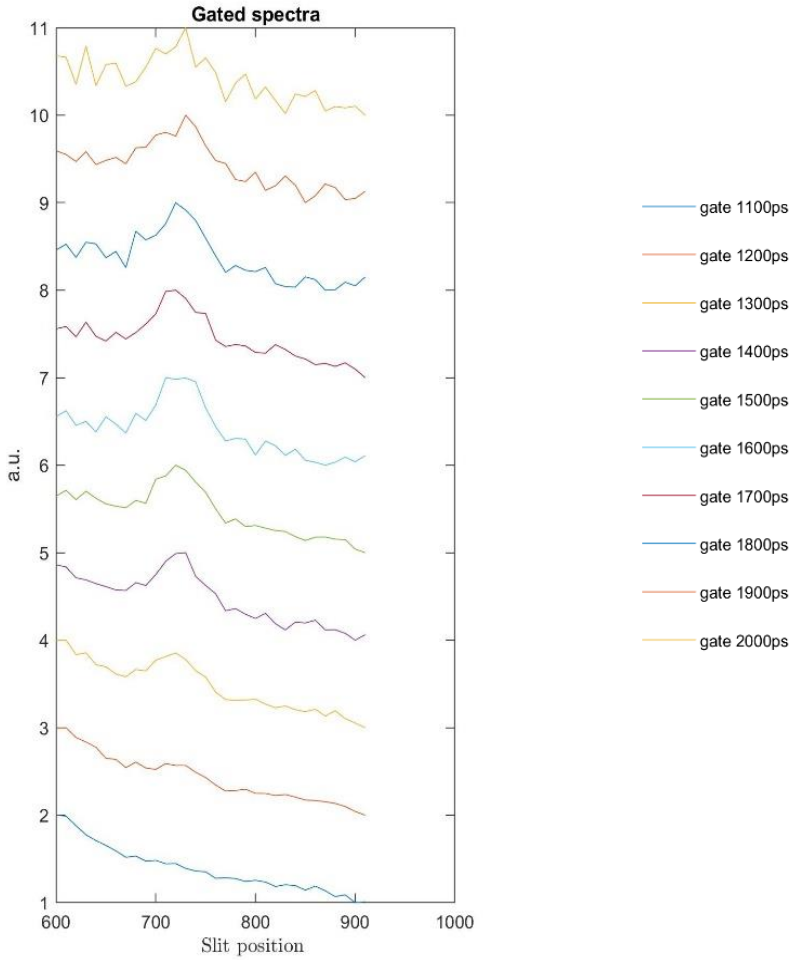

Fig. 58 Stack plot of the reconstructed raman spectra at different time gates. Early gates are shown on the mottom of the graph whilw late gates are on the top.

As it can be clearly seen, the Marble peak (bottom layer) is not present in early gates and, it appears at around 1300 ps in gate number three. Early gates show also a slight presence of the PMDS peaks. Unfortunately, PMDS peaks are also characterized by strong noise, therefore, are quite difficult to be recognized. To be considered that the reason of lower signal to noise ratio compared with the monochromator like measures is mainly due to lower integration times (one quarter from the previous one) and intrinsic noise is given by the Hadamard inverse transform.

6 CHAPTER 6 – CONCLUSIONS AND FUTURE PROSPECTIVE

6.1 DISCUSSION ON BEST OPTICAL LAYOUT

Configuration_1 shows a clear limitation in terms of efficiency and spectral resolution if compared with Configuration_2. The iris in Configuration_1 limits the optical efficiency of approximately 80% end the complexity of the alignment of the second branch makes it a less valuable option. Even though optical components of smaller size, make the system cheaper and more compact, the more relaxed tolerance in alignment in configuration_2, due to larger diameter lenses is preferred. Configuration_2 shows its negative side when it comes to DMD position. Due to the 45 degrees tilt of the DMD on its normal axis (in order to keep the beam on the propagation plane parallel to the table surface), the exploitable surface area is significantly reduced. As it can be seen in *[Fig. 60]*, if the DMD is tilted and the dispersion width unwinds on the vertical axis, the active area is just a reduced part of the whole DMD.

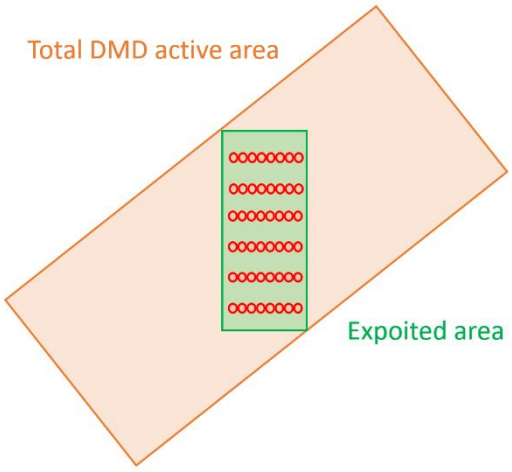

Fig. 59 Exploited DMD area (in green) in Configuration_2 , Inside the green area are shown the images of the fiber bundle at difference wavelengths . Dispersion dimension is on the vertical axis for this configuration.

As it can be seen in *[Fig. 60]* the loss of the exploitable surface of the DMD is very high. It implies a reduction of the maximum analyzable spectra. Even considering those drawbacks, Configuration_2 results in the best solution between the two. In *[Table 8]* are shown the features of the two configurations in comparison.

	Configuration_1	**Configuration_2**
f_number	f/4	f/2
Fiber Bundle	200 x 1400 µm	200 x 1400 µm
Grating (lines/mm)	300	300
Focal length	100 mm	100 mm
Lens diameter	25 mm	50 mm
Fondamental Resolution (nm/single pixel slit)	**0,241**	**0,174**
Absolute resolution (nm)	**6,20**	**5,26**
Efficiency	**2,37%**	**4%**

Table 8 Efficiency table of the two configuration. Resolution values have been calculated whereas values of optical efficiency have been measured.

6.2 Future Perspective

Thanks to this project it has been possible to build a homemade Compressive Sensing Time Domain spectrometer that exploits a single pixel detector for Raman spectroscopy applications. First measures have been conducted for TD CS Raman spectroscopy on bilayer phantoms with biological like optical properties. The time resolution of the spectrometer is approximately 180 ps and absolute spectral resolution of 5,26 nm.

The spectrometer can be strongly optimized by implementing a different kind of hardware updates. The most straightforward one is the use of a 50 x 1400 µm fiber bundle as input fiber. In this way, by lowering the image spot on the DMD plane it will be possible to have an increase of a factor of four

on the spectral resolution, giving a minimum resolvable bandwidth of 1.6 nm. Given the straightforwardness of this solution, it will be implemented in the nearest future.

It will be very important to optimize the filtering capabilities of the device. Excitation light is a big issue and in order to achieve a better dynamic range and signal to noise ratio, straight light must be eliminated. This could be accomplished by designing a better combination between color, interference and spatial filters used either in the probes or directly into the spectrometer. An upgrade in filtering quality of the apical elements will also help in obtaining the results wanted.

One other way to significantly increase the spectral resolution of the system will be to use a higher density line grating, in order to spread out the color dispersion on the DMD plane and achieve more spectral selectivity. In the optimal case with a 1200 line density grating and 50 µm lower dimension of the fiber bundle, it will possible to reach an absolute spectral resolution of 0.53 nm. Given the poor optical efficiency of the whole system, where the grating plays an important role, the implementation of a high-efficiency transmission grating will give a great improvement.

APPENDIX

MACROPROBE

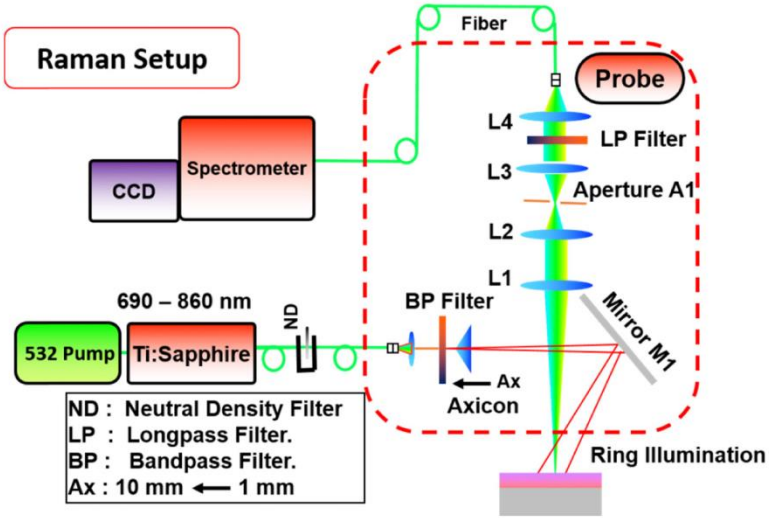

Fig. 60 Macroprobe demarked in dashed lines and complete experimental set up taken from

In *[Fig. 61]* it is possible to see the experimental setup including the Macroprobe, details, and pictures have been taken from [5].

The Ti:Sapphire laser, pumped by 532 nm light from a frequency doubled Nd:YAG laser, provides a tunable laser source in the 690-860 nm range. A 400 µm optical fiber couples the light from the laser to a collimator in the Raman probe, built using Thorlabs 30 mm diameter cage system. Depending on the excitation wavelength, a suitable 10 nm bandwidth bandpass filter (700 nm,750 nm, 780 nm, 810 nm) is used to clean the laser beam. An Axicon lens (UV fused silica axicon element with a cone angle $\alpha = 5°$) is then exploited to create ring illumination. Mirror M1 (silver mirror) reflects the ring source onto the sample. The radius of the ring illumination can be varied from 1 mm to 10 mm by moving the Axicon on its railing away from mirror M1. Cross positioning of mirror M1 and the corresponding incidence direction, slightly tilted with respect to normal incidence, distort only negligibly the shape of the ring *[Fig. 62]*. The source-detector separation d is calculated between the center of point collection and the inner radius of

ring illumination. The collection system involves a set of four optical lenses (diameter 25 mm) with effective f-number f/2. L2 and L3 along with a narrow aperture (A1) act as a Fourier optical low pass filter system, which enhances point collection and prevents stray light from entering the detection system. A suitable long pass filter (715 nm, 750 nm, 785 nm, 808 nm) is placed between lenses L3 and L4 to remove the excitation photons effectively. L4 couples the Raman signal into the optical fiber bundle, which transfers the light to the homemade spectrometer.

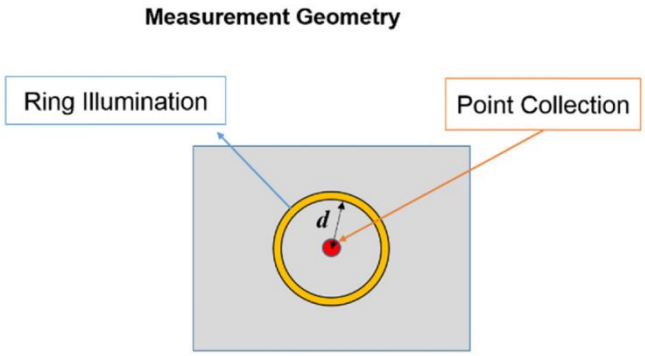

Fig. 61 Measurement geometry of the Macroprobe for diffusing media.

MICROPROBE

A microprobe, based on a 20× objective that allows analysis of a circular spot of 50 µm in diameter at a working distance of 3 mm. With the possibility to tune the position of the objective on the x y and z-axis with micrometric tolerance. Similar set up has been used in [36] and [53]. A sketch of the probe can be seen in *[Fig. 63]*

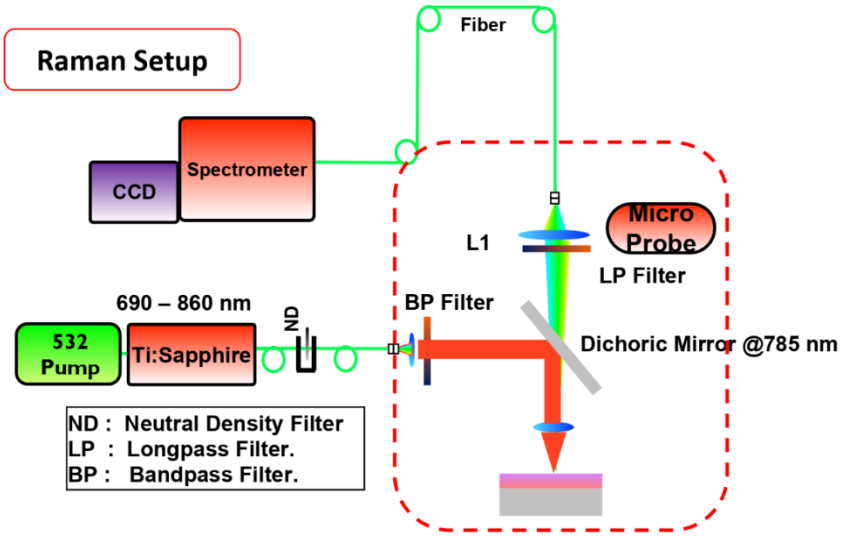

Fig. 62 Microprobe demarked in dashed lines and complete experimental set up taken from

TABLE OF FIGURES

BIBLIOGRAPHY

1. Taroni P, Pifferi A, Torricelli A, Comelli D, Cubeddu R. In vivo absorption and scattering spectroscopy of biological tissues. *Photochem Photobiol Sci*. 2003;2(2):124. doi:10.1039/b209651j
2. Contini D, Martelli F, Zaccanti G. Photon migration through a turbid slab described by a model based on diffusion approximation I Theory. *Appl Opt*. 1997. doi:10.1364/AO.36.004587
3. Martinenghi E, Di Sieno L, Tagliabue S, Mora AD, Farina A, Pifferi A. An innovative 8 channels system for time-resolved diffuse optical tomography based on SiPMs. In: *2016 IEEE Photonics Conference, IPC 2016*. ; 2017. doi:10.1109/IPCon.2016.7831149
4. Petry R, Schmitt M, Popp J. Raman Spectroscopy - A Prospective Tool in the Life Sciences. *ChemPhysChem*. 2003;4(1):14-30. doi:10.1002/cphc.200390004
5. Konugolu Venkata Sekar S, Mosca S, Farina A, et al. Frequency Offset Raman Spectroscopy (FORS) for subsurface probing of diffusive medium . *Eur Conf Biomed Opt*. 2017;25(Submitted):889-896. doi:10.1364/OE.25.004585
6. Okagbare PI, Esmonde-White FWL, Goldstein SA, Morris MD. Development of non-invasive Raman spectroscopy for in vivo evaluation of bone graft osseointegration in a rat model. *Analyst*. 2010. doi:10.1039/c0an00566e
7. Stone N, Baker R, Rogers K, Parker AW, Matousek P. Subsurface probing of calcifications with spatially offset Raman spectroscopy (SORS): Future possibilities for the diagnosis of breast cancer. *Analyst*. 2007. doi:10.1039/b705029a
8. Keller MD, Majumder SK, Mahadevan-Jansen A. Spatially offset Raman spectroscopy of layered soft tissues. *Opt Lett*. 2009. doi:10.1364/OL.34.000926
9. Olds WJ, Jaatinen E, Fredericks P, Cletus B, Panayiotou H, Izake EL. Spatially offset Raman spectroscopy (SORS) for the analysis and detection of packaged pharmaceuticals and concealed drugs. *Forensic Sci Int*. 2011. doi:10.1016/j.forsciint.2011.05.016
10. Heyler RA, Carriere JTA, Havermeyer F. THz-Raman – Accessing molecular

structure with Raman spectroscopy for enhanced chemical identification, analysis and monitoring. *ProcSPIE*. 2013. doi:10.1117/12.2018136

11. Kallaway C, Almond LM, Barr H, et al. Advances in the clinical application of Raman spectroscopy for cancer diagnostics. *Photodiagnosis Photodyn Ther*. 2013;10(3):207-219. doi:10.1016/j.pdpdt.2013.01.008
12. Matousek P, Towrie M, Ma C, et al. Fluorescence suppression in resonance Raman spectroscopy using a high-performance picosecond Kerr gate. *J Raman Spectrosc*. 2001. doi:10.1002/jrs.784
13. Efremov E V., Buijs JB, Gooijer C, Ariese F. Fluorescence rejection in resonance Raman spectroscopy using a picosecond-gated intensified charge-coupled device camera. *Appl Spectrosc*. 2007. doi:10.1366/000370207781269873
14. Van Duyne RP, Jeanmaire DL, Shriver DF. Mode-Locked Laser Raman Spectroscopy.A New Technique for the Rejection of Interfering Background Luminescence Signals. *Anal Chem*. 1974. doi:10.1021/ac60338a012
15. Martyshkin D V., Ahuja RC, Kudriavtsev A, Mirov SB. Effective suppression of fluorescence light in Raman measurements using ultrafast time gated charge coupled device camera. *Rev Sci Instrum*. 2004. doi:10.1063/1.1646743
16. Nissinen I, Nissinen J, Länsman AK, et al. A sub-ns time-gated CMOS single photon avalanche diode detector for Raman spectroscopy. In: *European Solid-State Device Research Conference*. ; 2011. doi:10.1109/ESSDERC.2011.6044156
17. Maruyama Y, Blacksberg J, Charbon E. A 1024×8 700ps time-gated SPAD line sensor for laser raman spectroscopy and LIBS in space and rover-based planetary exploration. In: *Digest of Technical Papers - IEEE International Solid-State Circuits Conference*. ; 2013. doi:10.1109/ISSCC.2013.6487659
18. Nissinen I, Nissinen J, Ker??nen P, L??nsman AK, Holma J, Kostamovaara J. A 2 ?? (4) ?? 128 multitime-gated SPAD line detector for pulsed Raman spectroscopy. *IEEE Sens J*. 2015. doi:10.1109/JSEN.2014.2361610
19. Kostamovaara J, Tenhunen J, Kögler M, Nissinen I, Nissinen J, Keränen P. Fluorescence suppression in Raman spectroscopy using a time-gated CMOS SPAD. *Opt Express*. 2013;21(25):31632. doi:10.1364/OE.21.031632
20. Mazurenka M, Jelzow A, Wabnitz H, et al. Non-contact time-resolved diffuse reflectance imaging at null source-detector separation " Effect of prolonged stimulation on cerebral hemodynamic: a time-resolved fNIRS study. *Opt Express*. 2012.
21. Ariese F, Meuzelaar H, Kerssens MM, et al. Deep Raman spectroscopy for the

non-invasive standoff detection of concealed chemical threat agents. *Front Optoelectron China*. 2011;94(4):349-358. doi:10.1016/j.talanta.2012.03.053

22. Ariese F, Meuzelaar H, Kerssens MM, Buijs JB, Gooijer C. Picosecond Raman spectroscopy with a fast intensified CCD camera for depth analysis of diffusely scattering media. *Analyst*. 2009. doi:10.1039/b821437a
23. Matousek P, Towrie M, Stanley A, Parker AW. Efficient rejection of fluorescence from Raman spectra using picosecond Kerr gating. *Appl Spectrosc*. 1999. doi:10.1366/0003702991945993
24. Wu J, Wang Y, Perelman L, Itzkan I, Dasari RR, Feld MS. 3-DIMENSIONAL IMAGING OF OBJECTS EMBEDDED IN TURBID MEDIA WITH FLUORESCENCE AND RAMAN-SPECTROSCOPY. *Appl Opt*. 1995. doi:10.1364/AO.34.003425
25. Iping Petterson IE, Dvořák P, Buijs JB, et al. Time-resolved spatially offset Raman spectroscopy for depth analysis of diffusely scattering layers. *Analyst*. 2010;135(12):3255-3259. doi:10.1039/c0an00611d
26. Konugolu Venkata Sekar S, Mosca S, Valentini G, Zuschratter W, Pifferi A, Milano P. Time Domain Diffuse Raman Instrumentation based on a TCSPC camera for depth analysis of diffusive media. *Opt Lett*. 2018. doi:10.1364/OL.43.002134
27. Martelli F, Binzoni T, Konugolu Venkata Sekar S, Farina A, Cavalieri S, Pifferi A. Time-domain Raman analytical forward solvers. *Opt Express*. 2016. doi:10.1364/OE.24.020382
28. Martelli F, Binzoni T, Konugolu Venkata Sekar S, Farina A, Cavalieri S, Pifferi A. Time-domain Raman analytical forward solvers. *Opt Express*. 2016;24(18):20382. doi:10.1364/OE.24.020382
29. Mccerry RL. *Raman Spectroscopy in Chemical Bioanalysis.*; 2000. doi:10.1002/0471721646
30. Hargreaves MD, Page K, Munshi T, Tomsett R, Lynch G, Edwards HGM. Analysis of seized drugs using portable Raman spectroscopy in an airport environment—a proof of principle study. *J Raman Spectrosc*. 2008. doi:10.1002/jrs.1926
31. Fortmeyer R. New airport security technology is slow to be implemented, but developments abound. *Archit Rec*. 2006.
32. Herrero AM. Raman spectroscopy a promising technique for quality assessment of meat and fish: A review. *Food Chem*. 2008. doi:10.1016/j.foodchem.2007.10.014
33. Li Y-S, Church JS. Raman spectroscopy in the analysis of food and pharmaceutical nanomaterials. *J Food Drug Anal*. 2014. doi:10.1016/j.jfda.2014.01.003

34. Conti C, Colombo C, Realini M, Matousek P. Subsurface analysis of painted sculptures and plasters using micrometre-scale spatially offset Raman spectroscopy (micro-SORS). *J Raman Spectrosc*. 2015. doi:10.1002/jrs.4673
35. Cheilakou E, Troullinos M, Koui M. Identification of pigments on Byzantine wall paintings from Crete (14th century AD) using non-invasive Fiber Optics Diffuse Reflectance Spectroscopy (FORS). *J Archaeol Sci*. 2014. doi:10.1016/j.jas.2013.09.020
36. Mosca S, Frizzi T, Pontone M, et al. Identification of pigments in different layers of illuminated manuscripts by X-ray fluorescence mapping and Raman spectroscopy. *Microchem J*. 2016. doi:10.1016/j.microc.2015.10.038
37. Zidan EH, Mosca S, Bellei S, et al. In situ imaging, elemental and molecular spectroscopy for the analysis of the construction and painting of a Late Period coffin at the Egyptian Museum of Cairo. *Meas J Int Meas Confed*. 2018. doi:10.1016/j.measurement.2017.11.055
38. Burgio L, Clark RJH, Muralha VSF, Stanley T. Pigment analysis by Raman microscopy of the non-figurative illumination in 16th- to 18th-century Islamic manuscripts. *J Raman Spectrosc*. 2008. doi:10.1002/jrs.2027
39. Kirsch M, Schackert G, Salzer R, Krafft C. Raman spectroscopic imaging for in vivo detection of cerebral brain metastases. *Anal Bioanal Chem*. 2010. doi:10.1007/s00216-010-4116-7
40. Krafft C, Belay B, Bergner N, et al. Advances in optical biopsy – correlation of malignancy and cell density of primary brain tumors using Raman microspectroscopic imaging. *Analyst*. 2012. doi:10.1039/c2an36083g
41. Rehman I, Smith R, Hench LL, Bonfield W. Structural evaluation of human and sheep bone and comparison with synthetic hydroxyapatite by FT-Raman spectroscopy. *J Biomed Mater Res*. 1995. doi:10.1002/jbm.820291016
42. Morris MD, Mandair GS. Raman assessment of bone quality. In: *Clinical Orthopaedics and Related Research*. ; 2011. doi:10.1007/s11999-010-1692-y
43. Kerns JG, Gikas PD, Buckley K, et al. Evidence from raman spectroscopy of a putative link between inherent bone matrix chemistry and degenerative joint disease. *Arthritis Rheumatol*. 2014. doi:10.1002/art.38360
44. Berto P, Scotté C, Galland F, Rigneault H, de Aguiar HB. Programmable single-pixel-based broadband stimulated Raman scattering. *Opt Lett*. 2017;42(9):1696. doi:10.1364/OL.42.001696
45. Arce GR, Brady DJ, Carin L, Arguello H, Kittle DS. Compressive coded aperture

spectral imaging: An introduction. *IEEE Signal Process Mag*. 2014;31(1):105-115. doi:10.1109/MSP.2013.2278763

46. Davis BM, Hemphill AJ, Cebeci Maltaş D, Zipper MA, Wang P, Ben-Amotz D. Multivariate hyperspectral raman imaging using compressive detection. *Anal Chem*. 2011;83(13):5086-5092. doi:10.1021/ac103259v
47. Lum DJ, Knarr SH, Howell JC. Fast Hadamard transforms for compressive sensing of joint systems : probability distribution. 2015;23(21):27636-27649. doi:10.1364/OE.23.027636
48. Tesi Pifferi - TiSapphire.pdf.
49. Farina A, Betcke M, di Sieno L, et al. Multiple-view diffuse optical tomography system based on time-domain compressive measurements. *Opt Lett*. 2017. doi:10.1364/OL.42.002822
50. A Correspondent. Using Lasers with DLP® DMD technology Purpose. *Nature*. 1968;218(5139):324-324. doi:10.1038/218324b0
51. Instruments T. Wavelength Transmittance Considerations for DLP - DMD Window. *Texas Instruments - Appl Rep*. 2012;(May):1-5. http://www.ti.com/lit/an/dlpa031c/dlpa031c.pdf.
52. Iping Petterson IE, Esmonde-White FWL, de Wilde W, Morris MD, Ariese F. Tissue phantoms to compare spatial and temporal offset modes of deep Raman spectroscopy. *Analyst*. 2015;140(7):2504-2512. doi:10.1039/C4AN01889C
53. Mosca S, Artesani A, Gulotta D, et al. Raman mapping and time-resolved photoluminescence imaging for the analysis of a cross-section from a modern gypsum sculpture. *Microchem J*. 2018. doi:10.1016/j.microc.2017.12.001